Radiation and Emission Characteristics of Laminar Partially-Premixed Flames of Petroleum Diesel-Canola Methyl Ester Blends

V. N. Singh*[1], R. N. Parthasarathy[2], S. R. Gollahalli[3]

School of Aerospace and Mechanical Engineering, University of Oklahoma

865 Asp Avenue, Norman, OK 73019, USA

*[1]Vinay.N.Singh-1@ou.edu; [2]rparthasarathy@ou.edu; [3]gollahal@ou.edu

Abstract

The primary objective of this study was to compare the effects of fuel-chemistry on the combustion properties of blends of Canola Methyl Ester (CME) and petroleum-based No.2 diesel in premixed flames at different initial equivalence ratios (1.2-7.0) in the fuel-rich regime. The fuel was vaporized and injected into a hot air stream and burned as a laminar flame at atmospheric pressure. The equivalence ratio was altered by changing the air flow rate. The flame appearance, global CO and NO emissions, and flame radiation were documented. The measured radiative heat fraction significantly increased with equivalence ratio. A decrease in the measured radiative heat fraction was observed as the volume percentage of CME was increased in the blend. The CME flames produced the highest emission index of NO, which declined as the volume percentage of CME was decreased in the fuel blend. In contrast, the diesel flame produced the highest emission index of CO, which decreased as the volume percentage of CME was increased in the blend.

Keywords

Diesel; Canola Methyl Ester; Combustion

Introduction

The increasing demand of petroleum fuels has resulted in a fast depletion of the natural petroleum resources and has sparked interest in the development of alternative fuels. Currently, 86 million barrels of oil are consumed world-wide per day; which is expected to increase to 121 million barrels a day by 2025, according to Pahl (2008). In 2009, petroleum accounted for 94 percent of the total use of energy in the transportation sector and was predicted to increase (US Department of Energy, 2010). The recent escalation of petroleum oil price has further prompted interest in fuel substitutes. Biofuels, such as canola methyl ester (CME), are viable alternatives to petroleum fuels, particularly for transportation, whose sources are renewable, locally grown, and free of sulfur and carbon-neutral. CME is produced by the transesterification of canola oil. Blends of CME and diesel can be readily used in current automobiles with minimal modifications. The use of such biofuels currently accounts for less than 1% of the total fuel consumption in the USA and Europe; in addition to cost considerations, the lack of detailed knowledge of the combustion behavior of biofuel blends is an inhibitor in the widespread use of these fuels.

In the last several decades, heavy-duty diesel engines have been regulated for smoke opacity, nitrogen oxides (NOx), particulate matter (PM), carbon monoxide (CO), and hydrocarbons (HC). Current standards specify emission limits for nonmethane hydrocarbons (NMHC) as well. The U.S. Environmental Protection Agency (EPA), in its national emissions inventory, estimated that diesel vehicles were responsible for 60% of on-road emissions of PM and 45% of on-road in 2000 (EPA report, 2003).

Several researchers have reported studies on exhaust emissions of diesel engines when operated using neat transesterified biofuels and their blends with diesel fuel. The results included a reduction in CO, smoke and PM, along with an increase in the oxides of nitrogen. Also, an increase in fuel consumption was observed due to the slightly lower energy content of biofuels compared to petroleum fuels. A number of fuel properties (viscosity, heating value, density and cetane number), as well as engine operating conditions have been shown to affect emissions from engines using biofuels.

Schumacher et al. (2001) compared the performance of two Detroit Diesel Corporation Series 60 engines that were fueled with various blends of biofuel and petroleum diesel fuel. The results of this study were in

agreement with those from previous studies on two and four stroke diesel engines; and an increase in NOx emissions, accompanied by a decrease in CO, particulate matter, and unburned hydrocarbons was observed. Canakci and Gerpen (2003) used petroleum diesel, yellow grease biofuel and soybean oil biofuel in a four–cylinder turbocharged diesel engine, at steady-state engine operating conditions. The use of both biofuels resulted in significant reductions in PM, CO, and unburned hydrocarbons. One of the studies (Labeckas and Salvinskas, 2006) showed the effects of rapeseed methyl ester (RME) on the exhaust emissions with a four-stroke, four-cylinder diesel engine. The engine was operated on neat RME and its 5%, 10%, 20% and 35% blends with diesel fuel. An increase in NOx emissions was observed with increasing engine speed; and the result was attributed to the increased mass percentage of oxygen in the biofuel.

Tsai et al. (2010) investigated the emissions of PM, total carbon (TC), e.g., organic/elemental carbons, and polycyclic aromatic hydrocarbons (PAHs) from a diesel generator fuelled with soy-biodiesel blends. Among the tested diesel blends (B0, B10 (10 vol% soy-biodiesel), B20, and B50), B20 exhibited the lowest PM emission concentration despite the loads (except the 5 kW case), whereas B10 displayed lower PM emission factors when operated at 0 and 10kW than other fuel blends. Fontaras et al. (2010) tested five biodiesels from different feedstocks (rapeseed, soy, sunflower, palm, and used fried oils) blended with diesel (10% by volume) on a Euro 3 common-rail passenger car and found that NOx emissions increased by up to 20% for two out of the five blends, decreased by up to 15% for two other blends, and remained unchanged for one blend; besides, PM was reduced for all blends by up to 25% and the reductions were positively correlated with the extent of biodiesel saturation. In general, pollutant emission studies in engines have shown that the majority of biofuels produced more NOx, less CO, PM, and unburned hydrocarbons than diesel fuel.

The aforementioned effects observed in engines are too complex to analyze, due to the interactions of engine design, operating conditions, and fluid-mechanics. To develop remedial steps, it is essential to separate the effects of fuel chemistry from those of engine variables. A flame technique has been developed by Love et al. (2009a) to isolate the effects of fuel chemistry on the combustion properties of biofuels. The partially-premixed laminar flames of prevaporized pure biofuels have been studied using this technique (Love et al., 2009b). The measured flame temperature and the soot volume fraction reported in these studies agreed well with those obtained from engine studies. Thus, the laminar flame arrangement provides a convenient venue to study the effects of only fuel composition and chemistry on the combustion properties.

The primary objective of this study was to compare the combustion characteristics of blends of CME, and petroleum-based No.2 diesel at varying equivalence ratios (Φ) of 1.2, 2, 3 and 7. The equivalence ratio is the ratio of the fuel-to-air mass ratio to the stoichiometric fuel-air mass ratio (Turns, 2000). Equivalence ratios greater than one signify rich fuel-air mixtures. These equivalence ratios were chosen to simulate the partially-premixed to non-premixed combustion zones that exist in the vicinity of the burning spray in diesel engines (not the overall equivalence ratio). The documented combustion characteristics include the flame appearance, the global emissions, and the total radiative fraction of heat release. The advantage of this method is that it provides a quick comparison of the major combustion properties (sooting tendencies and pollutant emissions) of various fuels, while utilizing small quantities of the fuel.

Experimental Set-Up and Methods

A description of the experimental set-up, instrumentation, fuels and test conditions is provided in this section.

Experimental Set-up

The experiments were conducted in a vertical steel test chamber with a cross section of 76x76 cm and height of 100 cm. The top of the combustion chamber was connected to the atmosphere through an exhaust duct. The ambient pressure in the laboratory was maintained slightly (20 Pa) above the atmospheric pressure, to provide a positive draft inside the test chamber and eliminate leakage of the combustion products into the main laboratory facility. High temperature heating tape with a proportional temperature controller was used to heat the flow lines carrying air to the desired temperature of 400^{o}C (which was close to the final boiling point of the liquid fuels) to completely vaporize the liquid fuels, without any coking. The liquid fuel was injected with a variable speed syringe pump and a 50 cm^{3} capacity syringe into the heated air (carrier gas) stream through

a high temperature silica-based septum. The vaporized fuel/air mixture was sent to a 9.5 mm inner diameter tube burner. The volumetric flow rate of the carrier gas was monitored using a calibrated rotameter. The feed line temperature was monitored using K-Type thermocouples. A schematic diagram of the experimental set-up is presented in Fig. 1. The vaporized fuel was ignited using a pilot flame, which was removed after ignition. The resulting flame was laminar (the burner exit Reynolds number was maintained below 120), whose characteristics were dependent on the chemistry of the fuel alone. The burner exit equivalence ratio was altered by changing the flow rate of air, while the fuel flow rate and thus energy input rate were constant.

Fuels

Three blends of CME with petroleum-based diesel were used: B25, B50 and B75 with 25%, 50% and 75% volume concentration of CME. The blends were prepared using a splash blending technique (Reid, 2007) in 5 US gallon (20 liter) amounts. In addition, pure CME and diesel were used to provide a baseline for comparison. The molecular formula, chemical composition and physical properties of No. 2 diesel fuel and canola methyl ester as well as the blends are presented in Table 1. A decrease in the heating value and an increase in the oxygen content are observed as the volume percentage of CME is increased in the blend. The large amount of air flow and length of the heated tube ensured that the vapors of the fuel components were well-mixed at the exit of the burner in spite of any preferential vaporization of the blend components.

Flame Visualization

Visible flame images were acquired using an 8 mega pixel digital AF SLR camera (EOS Digital Rebel XT/EOS 350D). The images were obtained under similar lighting conditions with a dark background at 1/25 second shutter speed. Using appropriate software, the number of pixels was counted and converted into length using a calibration reference.

Radiation Measurement

A wide view-angle (150^o) high sensitivity pyrheliometer was used to measure the radiation from the flame. The pyrheliometer was located far enough (50 cm) from the burner, so that its view-angle covered the entire flame length and the flame could be assumed as a point source. The pyrheliometer had a linear output with a sensitivity of 23.65 $W/m^2/mV$. A data acquisition board along with suitable software was used to sample the measured radiative heat flux. Each test was run for 3 min with a sampling rate of 1 Hz, allowing the heat flux to reach a steady value. The background radiation was subtracted from the total radiation measured to give the flame radiation (q). The radiative heat fraction was then computed using equation (1):

$$F=(4\pi\, l^2\, q)/(m\ LHV) \quad (1)$$

Here, l is the distance between the flame and pyrheliometer, m is the fuel mass flow rate and LHV is the lower heating value of the fuel. The radiative heat fraction characterizes the fraction of energy emitted from the flame in the form of radiation. Since most of the radiation in these flames is emitted by burning soot, the radiative heat fraction provides a convenient measure of the soot content in these flames.

Global Emissions

The emissions from the flame were measured by collecting gas samples through an uncooled quartz probe (1 mm diameter tip, expanding to a 6 mm ID tube) placed at the top of a pyrex flue gas collector. The pyrex flue gas collection funnel was placed 25 cm above the burner exit to collect the combustion products. Since the jet exit velocities were similar for all conditions, the entrainment and dilution was similar at this location for all fuels. Likewise, the temperature variation of the products was small. The flue gas collector and probe were aligned axially with the burner and the probe was placed above the flame. The gas samples were passed through a filter and ice-chilled water bath to remove particulates or moisture that might be present in the sample gas. A portable flue gas analyzer was used to measure the concentration of nitric oxide (NO), carbon dioxide (CO_2) and carbon monoxide (CO). The analyzer was calibrated with standard zero and reference gases before measurements were taken. The global emissions measurements were corrected to account for dilution of the product gases due to entrainment from ambient air. Therefore, the emission index (Turns, 2000) was used to characterize the pollutant emissions. The emission index expresses the amount of pollutant formed per unit mass of the fuel burnt:

$$EI_i = [X_i/ (X_{CO} + X_{CO2})]\ [(N\ MW_i)/MW_f] \quad (2)$$

Here X_i represents the mole fraction of species i, N is the number of carbon atoms in the fuel, and MW_i MW_f

are the molecular weight of species i and fuel respectively. It is assumed that all the carbon in the fuel is converted into CO or CO_2; which is reasonable because the soot content in the flames is small.

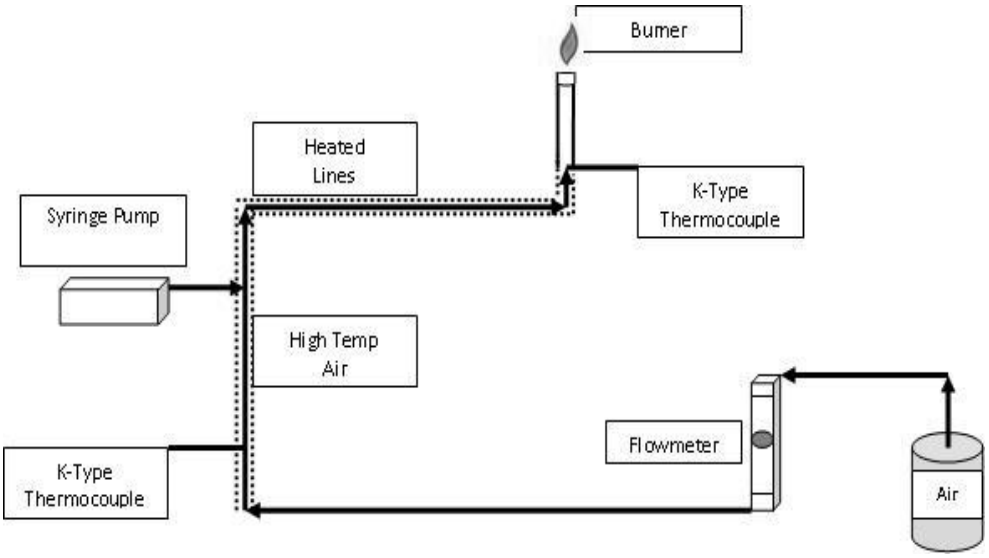

FIG. 1 SCHEMATIC DIAGRAM OF THE EXPERIMENTAL SET-UP

TABLE 1. FUEL PROPERTIES

Properties	Molecular Formula	Molecular Weight	Density (kg/m³)	LHV (MJ/kg)	Oxygen (Mass %)
Diesel	$C_{14.4}H_{24.9}$	197.7	843	42.6	0
CME B25	$C_{15.27}H_{27}O_{0.38}$	215.88	846	41.3	2.81
CME B50	$C_{16.28}H_{29.45}O_{0.82}$	237.97	853	40.0	5.51
CME B75	$C_{17.52}H_{32.42}O_{1.35}$	264.32	863	38.7	8.18
CME	$C_{19}H_{36}O_2$	296	876	37.4	10.81

Results and Discussion

Flame Appearance

The flames varied in color, structure, and length with change in equivalence ratio (Φ) that is the ratio of the stoichiometric air-fuel mass ratio to the actual air-fuel mass ratio. As the initial equivalence ratio was increased, less air was supplied, thus more air from the surroundings needed to be entrained, requiring an increase in length to effectively burn the fuel. A comparison of the flame images for CME B50 fuel at different equivalence ratios is provided in Fig. 2. As the equivalence ratio was increased from 1.2 to 7, the flame length increased from 4 to 20 cm. Also, the clear region near the injector became smaller. A visual comparison of the flames of various fuels at a constant equivalence ratio of 2 is presented in Fig. 3. It is observed that the flames of CME, diesel and the blends were similar in height and structure at the same equivalence ratio.

From the pictures, two primary regions were observed, a clear region (which appeared blue in color pictures) close to the injector exit and a luminous bright region in the flame away from the injector. The length of the clear region decreased as the volume percentage of CME in the blend was reduced. The near-injector clear zone represents the primary gas-phase oxidation reaction zone. In this region, the fuel-bound oxygen, in case of CME and its blends (Table 1), was available to participate in the oxidation of carbon monoxide and nitrogen, thus resulting in the blue hue observed at the base of the flame (Kitamura et al., 2001). The remaining unburned carbon continued to burn downstream with ambient oxygen, emitting continuum radiation at all wavelengths, thus appearing luminous yellow. At the same equivalence ratio, the diesel flame was the most luminous, with the luminosity decreasing as the CME concentration in the fuel was increased, indicating the presence of less soot in the flame with an increase in the CME content.

Global Radiation

The measured radiative heat fraction, presented in Fig.

4, significantly increased with equivalence ratio due to the increased soot formation as the exit fuel/air ratio became rich. The uncertainties in the measurements are presented as error bars. For each equivalence ratio studied, the diesel flame produced the highest value of radiative heat fraction; and a decrease in the measured radiative heat fraction was observed as the volume percentage of CME was increased in the fuel blend. The presence of fuel-bound oxygen in the CME blends played a significant role in the reduction of soot formation in these flames (as observed in the decrease in flame luminosity and increase in the near-injector homogeneous reaction zone in Figs. 2 and 3).

Global Emissions

The measured NO emission index for the fuels tested at the four equivalence ratios is presented in Fig. 5. The results indicate that the NO emissions decreased as the equivalence ratio was increased from $\Phi = 1.2$ to $\Phi = 7$ for all the fuels. For each equivalence ratio used, the pure CME flame produced the highest emission index of NO, followed by the CME B75, CME B50, and CME B25 flames and the lowest NO emission index was documented for the diesel flame.

In contrast, the CO emission index increased, as the equivalence ratio was increased from $\Phi = 1.2$ to $\Phi = 7$ for all fuels tested (as seen in Fig. 6). The diesel flame produced the highest emission index of CO followed by the CME B25, CME B50, CME B75 and CME flames at all equivalence ratios. These observations are similar to those documented during engine testing, as discussed earlier.

A high level of correlation among radiation, soot, and luminosity can be seen in the results presented above. The flames of CME biofuel and its blends produced lower radiation and CO emissions, but higher NO emissions than the diesel flame. The effect of additional oxygen in the molecular structure of CME and its blends contributes to the lower CO emissions and radiative heat emission. The production of low amounts of soot leads to less heat radiated, and higher temperatures, and consequently more thermal NO formation (Turns, 2000). Detailed in-flame measurements of temperature, soot volume concentrations and in-flame CO and NO concentrations are necessary to further understand the combustion characteristics of these flames.

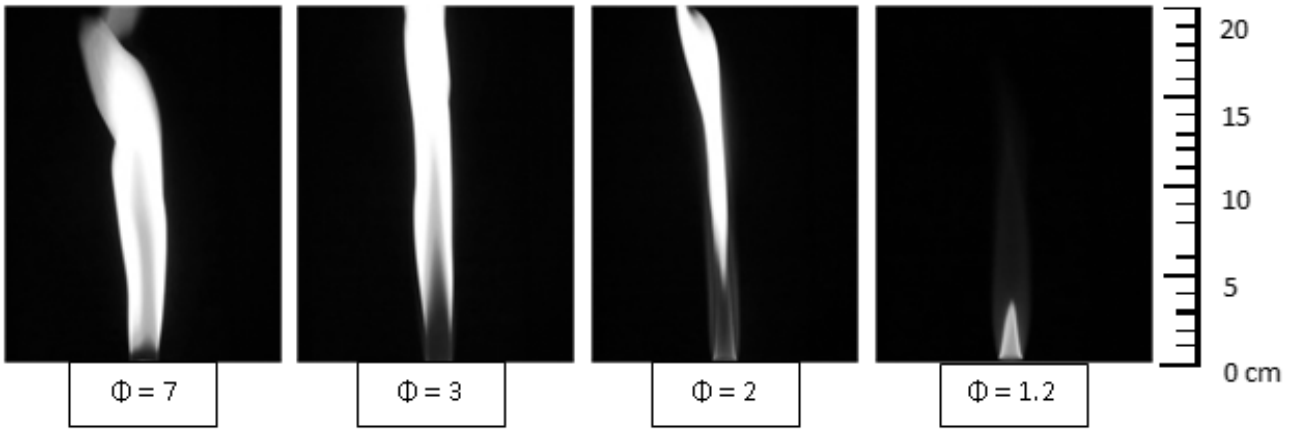

FIG.2. PHOTOGRAPHS OF CME B 50 FLAMES

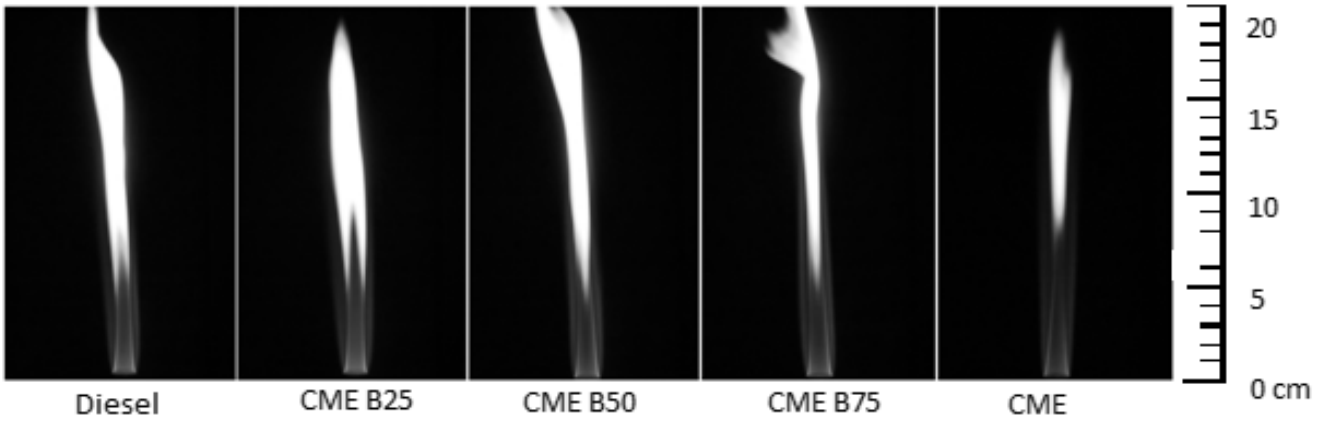

FIG.3. PHOTOGRAPHS OF FLAMES OF DIFFERENT FUELS AT AN EQUIVALENCE RATIO OF 2

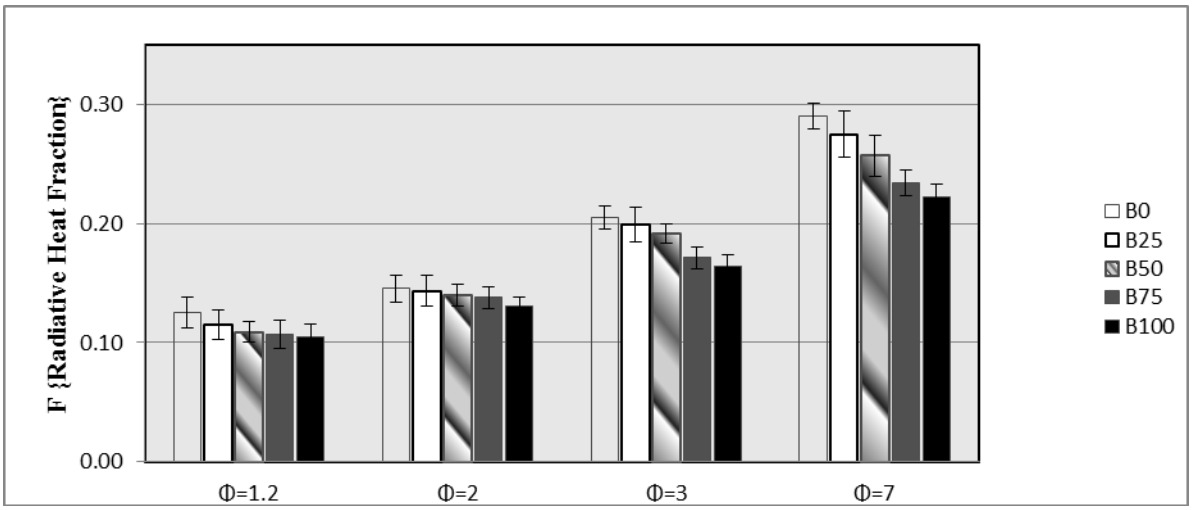

FIG.4. COMPARISON OF RADIATION FROM DIFFERENT FLAMES

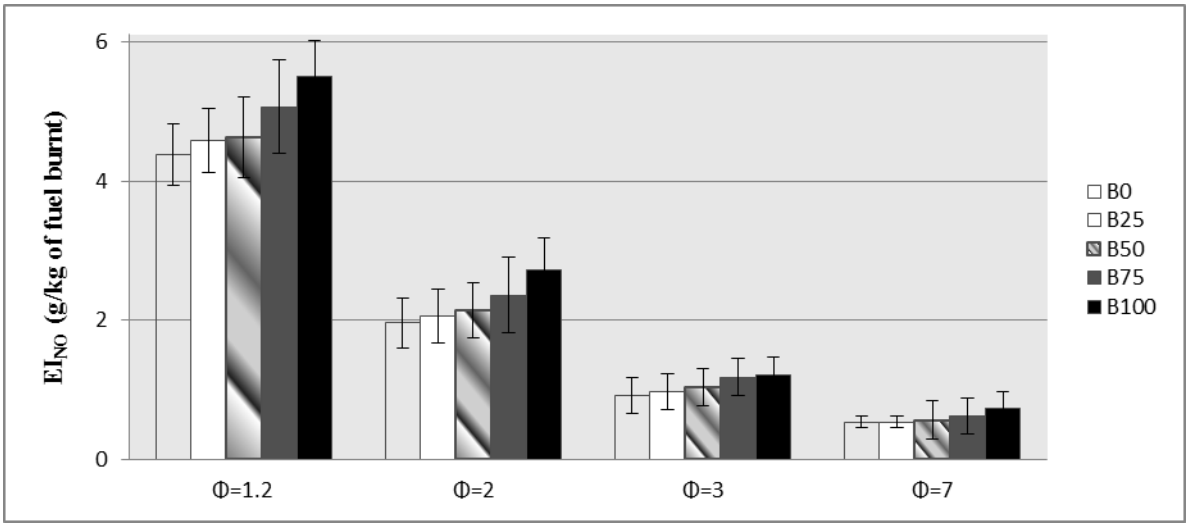

FIG.5. COMPARISON OF NO EMISSION INDEX OF DIFFERENT FLAMES

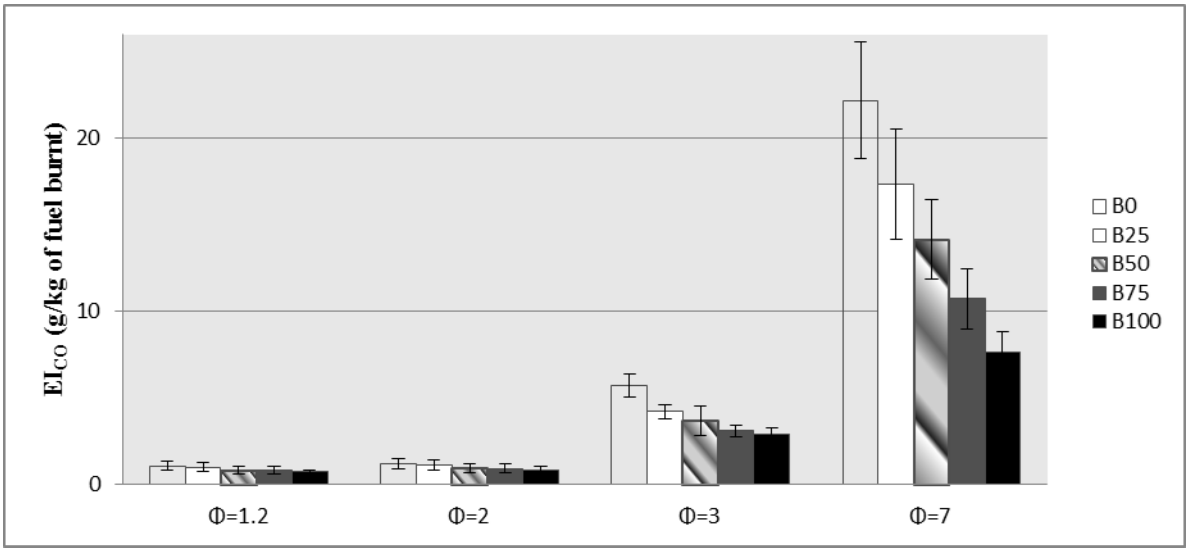

FIG.6. COMPARISON OF CO EMISSION INDEX OF DIFFERENT FLAMES

Conclusions

A method of rapid characterization of the soot/pollutant forming characteristics of fuels was used to investigate the effects of exit equivalence ratio on radiation and emissions in flames of petroleum diesel-CME blends. The following conclusions were drawn:

(a)For all fuels tested, the flame length decreased and the color changed from yellow to blue as the equivalence ratio was decreased from 7 to 1.2, indicating complete combustion close to stoichiometric air-fuel ratio.

(b)The radiative heat fraction and the CO emission index significantly rose with increasing equivalence ratio showing increased tendency of the flames to produce soot at higher equivalence ratios due to incomplete combustion. A decrease in radiative heat fraction and the emission index of CO was observed as the volume percentage of CME was increased in the blend due to the presence of oxygen in the molecular structure of the CME biofuel.

(c)The NO emissions decreased and the CO emissions increased as the equivalence ratio was increased from 1.2 to 7 for all fuels tested. An increment in the emission index of NO and a decrement in the CO emission index were observed as the volume percentage of CME was increased in the blend. While the presence of the fuel-bound oxygen can be attributed to the reduction in CO emission index, more measurements are needed to reveal the reasons behind the increased NO emission with the CME content of the fuel.

ACKNOWLEDGMENT

The financial support provided by NSF EPSCOR and US DoE is gratefully acknowledged.

REFERENCES

Canakci M. and Van Gerpen, J. “Comparison of Engine Performance and Emissions for Petroleum Diesel Fuel, Yellow Grease Biofuel and Soybean oil Biofuel” Transactions of the American Society of Agricultural and Biological Engineers 46 (2003): 937–944.

Fontaras, G. , Kousoulidou, M., Karavalakis, G., Tzamkiozis, T., Pistikopoulos, P., Ntziachristos, L, Bakeas, E., Stournas, S., and Samaras, Z. "Effects of Low Concentration Biodiesel Blend Application on Modern Passenger Cars. Part 1: Feedstock Impact on Regulated Pollutants, Fuel Consumption and Particle Emissions." Environmental Pollution 158 (2010): 1451-1460.

Kitamura T., Ito T., Senda J., and Fujimoto H. “Detailed Chemical Kinetic Modeling of Diesel Spray Combustion with Oxygenated Fuels.” SAE Technical Paper 2001-01-1262, (2001) doi:10.4271/2001-01-1262.

Labeckas, G. and Slavinskas, S. "The Effect of Rapeseed Oil Methyl Ester on Direct Injection Engine Performance and Exhaust Emissions." Energy Conversion and Management 47 (2006): 1954-1967.

Love N., Parthasarathy R. and Gollahalli S. “Rapid Characterization of Radiation and Pollutant Emissions of Biofuel and Hydrocarbon Liquid Fuels.” Journal of Energy Resources Technology 131 (2009a): 012202-1 – 012202-9.

Love, N. D., Parthasarathy, R. N. and Gollahalli, S. R. "Effect of Iodine Number on NOx Formation in Laminar Flames of Oxygenated Biofuels." International Journal of Green Energy 6 (2009b): 323-332.

Pahl, G. Biodiesel: Growing a New Energy Economy. Chelsea Green Publishing Company, 2008.

Reid, K. "Bioheat: Biofuel Oil in Focus - Part 1." Fuel Oil News (2007).

Schumacher L., Marshall W., Krahl J., Wetherell W. and Grabowski M. “Biofuel Emissions Data from Series 60 DDC Engines.” Transactions of the American Society of Agricultural and Biological Engineers 44 (2001): 1465–1468.

Tsai, J., Chen, S., Huang, K., Lin, Y., Lee, W., Lin, C., Lin, W. "PM, Carbon and PAH Emissions From a Diesel Generator Fuelled with Soy-Biodiesel Blends" Journal of Hazardous Materials 179 (2010): 237-243.

Turns S.. An Introduction to Combustion: Concepts and Applications, 2nd Edition, McGraw-Hill, 2000.

United States Department of Energy, "2009 Annual energy review," Washington DC : United States Department of Energy, 2010.

United States Environmental Protection Agency, "National air quality and emissions trends report, 2003," Special Studies Edition. Washington, DC : U.S. EPA, 2003

Modeling Oil and Petroleum Evaporation

Merv F. Fingas

Spill Science
1717 Rutherford Point, S.W., Edmonton, AB, Canada T6W 1J6
*[1]fingasmerv@shaw.ca

Abstract

Evaporation is an important component in oil spill models. Various approaches for oil evaporation prediction are summarized. Models can be divided into those models that use the basis of air-boundary-regulation or those that use liquid diffusion-regulated evaporation physics. Studies show that oil is not air boundary-layer regulated such as it is for water evaporation, which implies that a simplistic evaporation equation suffices to accurately describe the process. The following processes do not require consideration: wind velocity, turbulence level, area and scale size. The factors important to evaporation are time and temperature. Oil evaporation does show a thickness effect, although not as pronounced as that for air-boundary-layer regulated models. A thickness adjustment calculation is presented for diffusion-regulated models. This new model is applicable to thicknesses greater than about 1.5 mm. In the case of thin slicks, this adjustment is not relevant as oils typically spread to less than that in a short time.

The use of air-boundary-models results in three types of errors: air-boundary-layer models cannot accurately deal with long term evaporation; second, the wind factor results in unrealistic values and finally, they have not been adjusted for the different curvature for diesel-like evaporation. Further, these semi-empirical equations require inputs such as area, etc., that are unknown at the time of the spills. There has been some effort on the part of modellers to adjust air-boundary-layer models to be more realistic on the long-term, but these may be artificial and result in other errors such as under-estimation for long-term prediction. A comparison of models shows that on a very short term, such as a few hours, most models yield similar results. However, as time increases past a few days, the errors with air-boundary-layer regulated models are unacceptable. Examples are given where errors are as large as 100% over a few days.

Keywords

Oil Spill Evaporation; Hydrocarbon Evaporation; Evaporation Modeling

Introduction

Evaporation is an important process for most oil spills. Almost all oil spill models include evaporation as a process and output of the model. Evaporation plays a prime role in the fate of most oils. In a few days, typical crude oils can lose up to 45% of their volume (Fingas 2011). The Deepwater Horizon oil lost up to 55% in a short time when released under water at high pressure. Many crude oils must undergo evaporation before the formation of water-in-oil emulsions. Light oils will change very dramatically from fluid to viscous; while heavy oils will become solid-like. Many oils after long evaporative exposure, form tar balls or heavy tar mats. Despite the importance of the process, only some work has been conducted on the basic physics and chemistry of oil spill evaporation (Fingas 1995). The difficulty in studying oil evaporation is that oil is a mixture of hundreds of compounds and oil composition varies from source to source and even over time. Much of the work described in the previous literature focused on calibrating equations developed for water evaporation (Fingas 1995).

The mechanisms that regulate evaporation are important (Brutsaert 1995; Jones 1992). Evaporation of a liquid can be considered as the movement of molecules from the surface into the vapour phase above it. The immediate layer of air above the evaporation surface is known as the air boundary layer[5] which is the intermediate interface between the air and the liquid and might be viewed as very thin e.g. as less than 1 mm. The characteristics of this air boundary layer can influence evaporation. In the case of water, the boundary layer regulates the evaporation rate. Air can hold a variable amount of water, depending on temperature, as expressed by the relative humidity. Under conditions where the air boundary layer doesn't move (no wind) or has low turbulence, the air immediately above the water quickly becomes saturated and evaporation slows. The actual evaporation of water proceeds at a small fraction of the possible evaporation rate because of the saturation of the boundary layer. The air-boundary-layer physics is then said to regulate the evaporation of water. This regulation manifests the increase of evaporation with wind or turbulence. When

turbulence is weak, evaporation can slow down by orders-of-magnitude. The molecular diffusion of water molecules through air is at least 10^3 times slower than turbulent diffusion (Monteith and Unsworth 2008).

Some liquids are not air-boundary-layer regulated primarily because they evaporate too slowly to make the vapours saturate the air boundary layer above them (Fingas 2011). Many mixtures are regulated by the diffusion of molecules inside the liquid to the surface of the liquid. Such a mechanism is true for many slowly-evaporating mixtures of compounds such as oils and fuels. Some of the outcomes of this mechanism may seem counterintuitive to some people such as that increasing area may not necessarily increase evaporation rate. More importantly, increasing wind speed does not increase evaporation.

Scientific work on water evaporation dates back decades and thus the basis for early oil evaporation work has been established (Fingas 2011). There are several fundamental differences between the evaporation of a pure liquid such as water and that of a multi-component system such as crude oil. The evaporation rate for a single liquid such as water is a constant with respect to time. Evaporative loss, either by weight or volume, is not linear with time for crude oils, and other multi-component fuel mixtures (Fingas 1997).

Review of Historical Developments

For air-boundary-layer regulated liquids, one can write the mass transfer rate in semi-empirical form as (Fingas 2011):

$$E = K C T_u S \quad (1)$$

where E is the evaporation rate in mass per unit area, K is the mass transfer rate of the evaporating liquid, sometimes denoted as k_g (gas phase mass transfer coefficient, which may incorporate some of other parameters noted here), C is the concentration (mass) of the evaporating fluid as a mass per volume, T_u is a factor characterizing the relative intensity of turbulence, and S is a factor related to the saturation of the boundary layer above the evaporating liquid. The saturation parameter, S, represents the effects of local advection on saturation dynamics. If the air has already been saturated with the compound in question, the evaporation rate approaches zero. This also relates to the scale length of an evaporating pool. If one views a large pool over which a wind is blowing, there is a high probability that the air is saturated downwind and the evaporation rate per unit area is lower than that for a smaller pool. It is noted that there are many equivalent ways to express this fundamental evaporation equation. These will be seen in the equations below.

Sutton proposed the following equation based on empirical work (Brutsaert 1982):

$$E = K C_s U^{7/9} d^{-1/9} Sc^{-r} \quad (2)$$

where C_s is the concentration of the evaporating fluid (mass/volume), U is the wind speed, d is the area of the pool, Sc is the Schmidt number and r is the empirical exponent assigned values from 0 to 2/3. Other parameters are defined as above. The terms in this equation are analogous to the very generic equation, (1), proposed above. The turbulence is expressed by a combination of the wind speed, U, and the Schmidt number, Sc that is the ratio of kinematic viscosity of air (ν) to the molecular diffusivity (D) of the diffusing gas in air, i.e., a dimensionless expression of the molecular diffusivity of the evaporating substance in air.[7] The coefficient of the wind power typifies the turbulence level. The value of 0.78 (7/9) as chosen by Sutton, represents a turbulent wind whereas a coefficient of 0.5 would represent a wind flow that is more laminar. The scale length represented by d has been given an empirical exponent of -1/9. This represents for water, a weak dependence on size. The exponent of the Schmidt number, r, represents the effect of the diffusivity of the particular chemical, and historically was assigned values between 0 and 2/3 (Sutton 1934).

Blokker was the first to develop oil evaporation equations for oil evaporation at sea, with his partially theoretical starting basis (Blokker, 1964). Oil was presumed to be a one-component liquid. The distillation data and the average boiling points of successive fractions were used as the starting point to predict an overall vapour pressure. The average vapour pressure of these fractions was then calculated from the Clausius-Clapeyron equation to yield:

$$\log \frac{p_s}{p} = \frac{qM}{4.57}\left(\frac{1}{T} - \frac{1}{T_s}\right) \quad (3)$$

where p is the vapour pressure at the absolute temperature, T; p_s is the vapour pressure at the boiling point, T_s (for p_s, 760 mm Hg was used); q is the heat of evaporation in cal/g and M is the molecular weight.

The term $qM/(4.57\ T_s)$ was taken to be nearly constant

for hydrocarbons (=5.0 +/- 0.2) and thus the expression was simplified to

$$\log p_s/p = 5.0\,[(T_s - T)/T] \quad (4)$$

From the empirical data and equation (4), the weathering curve was calculated, assuming that Raoult's law is valid for this situation giving qM as a function of the percentage evaporated. Pasquill's equation was applied stepwise, and the total evaporation time was obtained by summation:

$$t = \frac{\Delta h D^{\beta}}{K_{ev}\, U^{\alpha}} \sum \frac{1}{PM} \quad (5)$$

where t is the total evaporation time in hours, Δh is the decrease in layer thickness in m, D is the diameter of the oil spill, β is a meteorological constant (assigned a value of 0.11), K_{ev} is a constant for atmospheric stability (taken to be 1.2×10^{-8}), α is a meteorological constant (assigned a value of 0.78), P is the vapour pressure at the absolute temperature, T; and M is the molecular weight of the component or oil mass. Tests of this equation by experimental evaporation using a small wind tunnel did not yield good correspondence to test data.

Mackay and Matsugu (1973) approached evaporation by using the classical water evaporation and experimental work. The water evaporation equation was corrected to hydrocarbons using the evaporation rate of cumene. Data on the evaporation of water and cumene have been used to correlate the gas phase mass transfer coefficient as a function of wind-speed and pool size by the equation,

$$K_m = 0.0292\, U^{0.78}\, X^{-0.11}\, Sc^{-0.67} \quad (6)$$

Where K_m is the mass transfer coefficient in units of mass per unit time and X is the pool diameter or the scale size of evaporating area. Note that the exponent of the wind speed, U, is 0.78 equal to the classical water evaporation-derived coefficient. Mackay and Matsugu noted that for hydrocarbon mixtures the evaporation process is more complex, dependent on the liquid diffusion resistance being present.[9] Experimental data on gasoline evaporation were compared with computed rates which showed some deviations from the experimental values and suggested the presence of a liquid-phase mass-transfer resistance. The same group showed that the evaporative loss of a mass of oil spilled can be estimated using a mass transfer coefficient, K_m, as shown above (Goodwin et al. 1976). This approach was investigated with some laboratory data and tested against some known mass transfer conditions on the sea Butler (1976) developed a model to examine evaporation of specific hydrocarbon components. The weathering rate was taken as proportional to the equilibrium vapour pressure, P, of the compound and to the fraction remaining:

$$dx/dt = -kP(x/x_o) \quad (7)$$

where x is the amount of a particular component of a crude oil at time, t, x_o is the amount of that same component present at the beginning of weathering (t = 0), k is an empirical rate coefficient and P is the vapour pressure of the chosen oil component.

Butler assumed that petroleum is a complicated mixture of compounds, therefore P is not equal to the vapour pressure of the pure compound, but neither would there be large variation in the activity coefficient as the weathering process occurs (Butler 1976). For this reason, the activity coefficients were subsumed in the empirical rate coefficient k. P and k were taken as independent of the amount, x, for a fairly wide range of oils. The equation was then directly integrated to give the fraction of the original compound remaining after weathering as:

$$x/x_o = \exp(-ktP/x_o) \quad (8)$$

The vapour pressure of individual components was fit using a regression line to yield a predictor equation for vapour pressure:

$$P = \exp(10.94 - 1.06\,N) \quad (9)$$

where P is the vapour pressure in Torr and N is the carbon number of the compound in question. This combined with equation (8) and yielded the following expression:

$$x/x_o = \exp\,[-(kt/x_o)\exp(10.94 - 1.06\,N)] \quad (10)$$

Where x/x_o is the fraction of the component left after weathering, k is an empirical constant, x_o is the original quantity of the component and N is the carbon number of the component in question. Equation (10) predicts that the fraction weathered is a function of the carbon number and decreases at a rate that is faster than predicted from simple exponential decay.[12] If the initial distribution of compounds is essentially uniform (x_o independent of N), then the above equation predicts that the carbon number where a constant fraction (e.g. half) of the initial amount has been lost ($x = 0.5\,x_o$) is a logarithmic function of the time of weathering:

$$N_{1/2} = 10.66 + 2.17 \log (kt/x_o) \quad (11)$$

where $N_{1/2}$ is half of the volume fraction of the oil. The equation was tested using evaporation data from some patches of oil on shoreline, whose age was known. The equation was capable of predicting the age of the samples relatively well. It was suggested that the equation was applicable to open water spills; however, this was never subsequently applied in models.

Yang and Wang (1977) developed an equation using the Mackay and Matsugu molecular diffusion process.[2] The vapour phase mass transfer process was expressed as:

$$D_{ie} = \frac{k_m (p_i - p_{i\infty})}{[RT_s]} \quad (12)$$

where D_{ie} is the vapour phase mass transfer rate, k_m is a coefficient that lumps all the unknown factors affecting the value of D_{ie}, p_i is the hydrocarbon vapour pressure of fraction, I, at the interface, $p_{i\infty}$ is the hydrocarbon vapour pressure of fraction, I, at infinite altitude of the atmosphere, R is the universal gas constant and T_s is the absolute temperature of the oil slick. The following functional relationship was proposed (Yang and Wang 1977):

$$k_m = \alpha A^{\gamma} e^{qU} \quad (13)$$

where A is the slick area, U is the over-water wind speed, and *a*, q and γ are empirical coefficients. This relationship was based on the results of previous studies, including, for instance, those of MacKay and Matsugu who suggested the value of γ to be in the range from -0.025 to -0.055.[9] Further experiments were performed by Yang and Wang to determine the values of '*a*' and 'q'. Experiments showed that a film formed on evaporating oils and this film severely retarded evaporation. Before the surface film has developed ($\varrho_t/\varrho_o < 1.0078$):

$$K_{mb} = 69\, A^{-0.0055}\, e^{0.42U} \quad (14)$$

where K_{mb} is the coefficient that groups all factors affecting evaporation before the surface film has formed and A is the area. After the surface film has developed ($\varrho_t/\varrho_o > 1.0078$)

$$K_{ma} = 1/5\, k_{mb} \quad (15)$$

where ϱ_o is initial oil density, ϱ_t is weathered oil density at time t, and K_{ma} is the coefficient that groups all factors affecting evaporation after the surface film has formed.[12] The evaporation rate was found to be reduced fivefold after the formation of the surface film.

Drivas (1982) compared the Mackay and Matsugu equation with data found in the literature and noted that the equations yielded predictions that were close to the experimental data. Rheijnhart and Rose (1982) developed a simple predictor model for the evaporation of oil at sea and proposed the following simple relationship:

$$Q_{ei} = \alpha C_o \quad (16)$$

where Q_{ei} is the evaporation rate of the component of interest, α is a constant incorporating wind velocity and other factors (taken as 0.0009 m s^{-1}) and C_o is the equilibrium concentration of the vapour at the oil surface. Several pan experiments were run to simulate evaporation at sea and the data used to test the equation. No method was given to calculate the essential value, C_o.

Brighton (1985,1990) proposed that the standard formulation used by many workers required refining. His starting point for water evaporation was similar to that proposed by Sutton:

$$E = K_m C_s U^{7/9} d^{1/9} Sc^{r} \quad (17)$$

where E is the mean evaporation rate per unit area, K_m is an empirically-determined constant, presumably related to the foregoing mass transfer constant, C_s is the concentration of the evaporation fluid (mass/volume), d is the area of the pool and r is an empirical exponent assigned values from 0 to 2/3. Brighton suggested that this equation should conform to the basic dimensionless form involving the parameters U and Zo (wind speed and roughness length, respectively) which define the boundary layer conditions. The key factor in Brighton's analysis was to use a linear eddy-diffusivity profile. This feature implied that concentration profiles become logarithmic near the surface, which is suspected to be more realistic compared to the more finite values previously used. Using a power profile to provide an estimation of the turbulence, Brighton was able to substitute the following identities into the classical relationship:

$$U = \frac{u^*}{k} n \quad (18)$$

$$n = \left(\ln \frac{z_1}{z_0}\right) \quad (19)$$

Where: u* is the friction velocity, z_1 is the reference height above the surface, z_0 is the roughness length and n is the power law dimensionless term. The evaporation equation now became:

$$U\left(\frac{z}{z_1}\right)\frac{\delta X}{\delta x} = \frac{\delta}{\delta z}\left(\frac{k\, u^*\, z}{\sigma}\right)\left(\frac{\delta X}{\delta z}\right) \quad (20)$$

where z is the height above the surface, X is the concentration of the evaporating compounds, x is the dimension of the evaporating pool, k given by K/u*z, is the von Karman constant and σ is the turbulent Schmidt number (taken as 0.85). Brighton subsequently compared his model with experimental evaporation data in the field and in the laboratory, including laboratory oil evaporation data (Brighton 1985, 1990). The model only correlated well with laboratory water evaporation data and the reason given was other data sets were 'noisy'.

Tkalin (1986) proposed a series of equations to predict evaporation at sea:

$$E_i = \frac{K_a M_i P_{oi} x_t}{RT} \quad (21)$$

where E_i is the evaporation rate of component I (or the sum of all components) (kg/m^{2}s), K_a is the mass transfer coefficient (m/s), M_i is the molecular weight, P_{oi} is the vapour pressure of the component I, and x_t is the amount of component I at time, t. Using empirical data, relationships were developed for some of the factors in the equation:

$$P_{oi} = 10^3 e^A \quad (22)$$

where $A = -(4.4 + \log T_b)[1.803\{T_b/T - 1\} - 0.803 \ln(T_b/T)]$ (23)

and where T_b is the boiling point of the hydrocarbon, given as

$$K_a = 1.25U10^{-3} \quad (24)$$

The equations were verified using empirical data from the literature.

A frequently used work in older spill modelling is that of Stiver and Mackay (1984)based on some of the earlier work of Mackay and Matsugu (1973). The formulation was initiated with assumptions on the evaporation of a liquid. If a liquid is spilled, the rate of evaporation is given as:

$$N = KAP/(RT) \quad (25)$$

where N is the evaporative molar flux (mol/s), K is the mass transfer coefficient under the prevailing wind (ms^{-1}) and A is the area (m^2), P is the vapour pressure of the bulk liquid. This equation was arranged to give:

$$dF_v/dt = KAP\nu/(V_oRT) \quad (26)$$

where F_v is the volume fraction evaporated, v is the liquid's molar volume (m^3/mol) and V_o is the initial volume of spilled liquid (m^3). By rearranging:

$$dF_v = [P\nu/(RT)](KAdt/V_o) \quad (27)$$

$$\text{or} \quad dF_v = Hd\theta \quad (28)$$

where H is Henry's law constant and θ is the evaporative exposure (defined below).

The right-hand side of the second last equation has been separated into two dimensionless groups (Stiver and MacKay 1984). The group, KAdt/V_o, represents the time-rate of what has been termed as the "evaporative exposure" and was denoted as dθ. The evaporative exposure is a function of time, the spill area and volume (or thickness), and the mass transfer coefficient (which is dependent on the wind speed). The evaporative exposure can be viewed as the ratio of exposed vapour volume to the initial liquid volume.[18]

The group Pν/(RT) or H is a dimensionless Henry's law constant or ratio of the equilibrium concentration of the substance in the vapour phase [P/(RT)] to that in the liquid (l/ν). H is a function of temperature. The product θH is thus the ratio of the amount which has evaporated (oil concentration in vapour times vapour volume) to the amount originally present. For a pure liquid, H is independent of F_v and equation 26 was integrated directly to give:

$$F_v = H\,\theta \quad (29)$$

If K, A, and temperature are constant, the evaporation rate is constant and evaporation is complete (F_v is unity) when θ achieves a value of 1/H.

If the liquid is a mixture, H depends on F_v and the basic equation can only be integrated if H is expressed as a function of F_v; i.e., the principal variable of vapour pressure is expressed as a function of composition. The evaporation rate slows as evaporation proceeds in such cases. Equation (27) was replaced with a new equation developed using laboratory empirical data:

$$F_v = (T/K_1) \ln (1 + K_1\theta/T) \exp(K_2 - K_3/T) \quad (30)$$

where F_v is the volume fraction evaporated and $K_{1,2,3}$ are empirical constants.[18] A value for K_1 was obtained from the slope of the F_v vs. log θ curve from pan or bubble evaporation experiments. For θ greater than 10^4, K_1 was found to be approximately 2.3T divided by the slope. The expression exp(K_2 - K_3/T) was then calculated, and K_2 and K_3 were determined individually from evaporation curves at two different temperatures.

Hamoda and co-workers (1989) performed theoretical and experimental work on evaporation. An equation

was developed to express the effects of API° (American Petroleum Institute gravity-a unit of density) of the crude oil, temperature, and salinity on the mass transfer coefficient K:

$$K = 1.68 \times 10^{-5} (API^{o})^{1.253} (T)^{1.80} e^{0.1441} \quad (31)$$

where K is the mass transfer coefficient, cm h^{-1}, API° is the density in API units, unitless, and e is the water salinity in degrees salinity or parts-per-thousand. The exponents of the equation were determined by multiple linear regression on experimental data.

Quinn and co-workers (1990) weathered oils in a controlled environment and correlated the data with equations developed starting with Fick's diffusion law and the Clausius-Clapeyron equation. Crude oil was divided into a series of pseudo fractions by boiling point. Each fraction was taken to be equivalent to an n-paraffin. The n-paraffin distributions of a number of naturally weathered crude oils were determined by capillary gas-liquid chromatography. The actual measured evaporation was compared with those generated by computer simulation of weathering.

Bobra (1992) conducted laboratory studies on the evaporation of crude oils. The evaporation curves for several crude oils and petroleum products were measured under several different environmental conditions. These data were compared to the equation developed by Stiver and Mackay (1984). The equation used was:

$$F_V = \ln[1 + B(T_G/T)\ \theta \exp(A - B\ T_o/T)]\ \{T/BT_G\} \quad (32)$$

where F_V is the fraction evaporated, T_G is the gradient of the modified distillation curve, A and B are dimensionless constants, T_o is initial boiling point of the oil and θ is the evaporative exposure as previously defined. The constants for the above equation and the results from several comparison runs were carried out.[21] The agreement between the experimental data and the equation results were poor in most cases. This comparison showed that the Stiver and Mackay equation predicts the evaporation of most oils relatively well until time approaches 8 hours, after that it over-predicted the evaporation. The 'overshoot' could be as much as 10% evaporative loss at the 24-hour mark. This is especially true for very light oils. The Stiver and Mackay equation was also found to under-predict or over-predict the evaporation of oils in the initial phases. Bobra also noted that most oil evaporation follows a logarithmic curve with time and that a simple approach to this was much more accurate than using equation (30).

In summary, it is difficult to develop a theoretical approach to oil evaporation for several reasons. First, oil consists of many components and thus there is no constant boiling point, vapor pressure or other essential properties used in typical evaporation models. Further, oil evaporation proceeds by diffusion regulation but not by air-boundary-layer regulation. Water evaporation models cannot be accurately modified to oil evaporation for these reasons.

Development of Diffusion-Rgulated Models

The review of the predictive and theoretical work in section 2 above reveals those air-boundary-layer concepts that are limited and cannot accurately explain long-term evaporation. Fingas conducted a series of experiments over several years to examine the concepts (Fingas 1998, 2011).

Wind Experiments

A simple experiment to determine whether or not oil evaporation is air-boundary-layer regulated is to measure if the evaporation rate increases with wind as predicted by equations (2) and (6) above. Experiments on the evaporation of oil with and without winds were conducted with ASMB (Alberta Sweet Mixed Blend), gasoline, and with water. Water formed a baseline data set since this is the substance being compared.[4] Regressions on the data were performed and the equation parameters calculated. Curve coefficients are the constants from the best fit equation [Evap = a ln(t)], t=time in minutes, for logarithmic equations or Evap=a √t, for the square root equations. Oils such as diesel fuel with fewer sub-components evaporating at one time, have a tendency to fit square root curves (Fingas 2011, Li et al. 2004). While data were calculated separately for percentage of weight lost and absolute weight, the latter are usually used because it is more convenient. The plots of wind speed versus the evaporation rate (as a percentage of weight lost) for each oil type are shown in Figures 1 to Figure 3. These figures show that the evaporation rates for oils and even the light product, gasoline, are not increased with increasing wind speed. The evaporation rate after the 0-wind value is nearly identical for all oils, resulting from the stirring effect on the oil which increases the diffusion rate to the surface. Stirring will increase the diffusion and therefore the evaporation rate. The oil evaporation data can be compared to the evaporation of water, as illustrated in Figure 4. These data show the classical relationship of the water evaporation rate correlated with the wind speed (evaporation varies as

$U^{0.78}$, where U is wind speed). This comparison shows that the oils studied here are not air boundary-layer regulated.

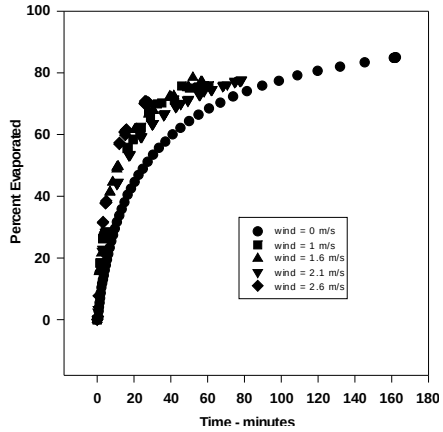

FIG. 1 EVAPORATION OF GASOLINE WITH VARYING WIND VELOCITIES. THIS FIGURE ALSO SHOWS THAT THERE IS LITTLE VARIATION WITH WIND VELOCITY EXCEPT IN GOING FROM THE 0-WIND-LEVEL UP TO THE OTHERS. THIS IS DUE TO THE STIRRING EFFECT OF WIND AND NOT AIR-BOUNDARY LAYER REGULATION.

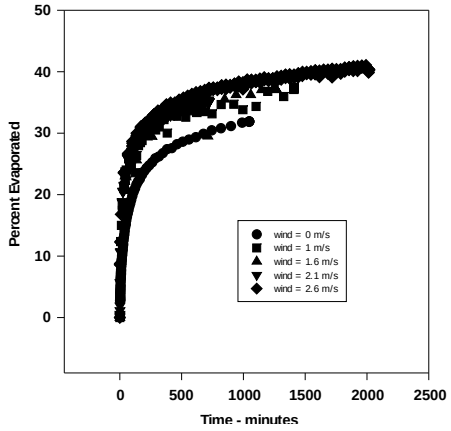

FIG. 2 VAPORATION OF ALBERTA LIGHT CRUDE OIL WITH VARYING WIND VELOCITIES. THIS FIGURE SHOWS THAT THERE IS LITTLE VARIATION WITH WIND VELOCITY EXCEPT IN GOING FROM THE 0-WIND-LEVEL UP TO THE OTHERS. THIS IS DUE TO THE STIRRING EFFECT OF WIND AND NOT AIR-BOUNDARY LAYER REGULATION.

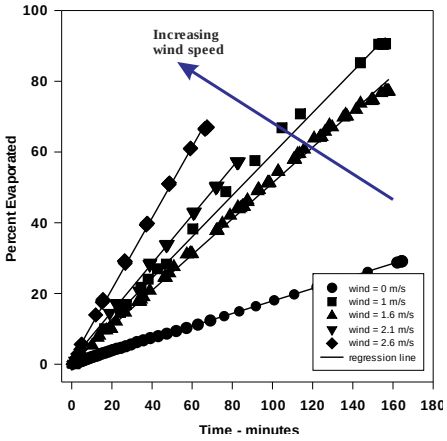

FIG. 3 EVAPORATION OF WATER WITH VARYING WIND VELOCITIES. THIS FIGURE SHOWS DRAMATIC DIFFERENCES IN THE EVAPORATION RATE OF WATER WITH WIND VELOCITY. THIS IS TYPICAL OF AIR-BOUNDARY-LAYER REGULATION. COMPARE FIGURE 3 WITH OIL EVAPORATION IN FIGURES 1 AND 2 WHICH DO NOT SHOW THIS TREND OF VARIANCE WITH WIND VELOCITY.

Figure 4 shows the rates of evaporation compared to the wind speed for all the liquids used in the study, as well as the evaporation rates of all test liquids versus wind speed. The lines shown are those calculated by linear regression. This clearly shows that water evaporation rate increased, as expected, with increasing wind velocity. The oils, ASMB (Alberta Sweet Mixed Blend) and gasoline, do not show rises with increasing wind speed.

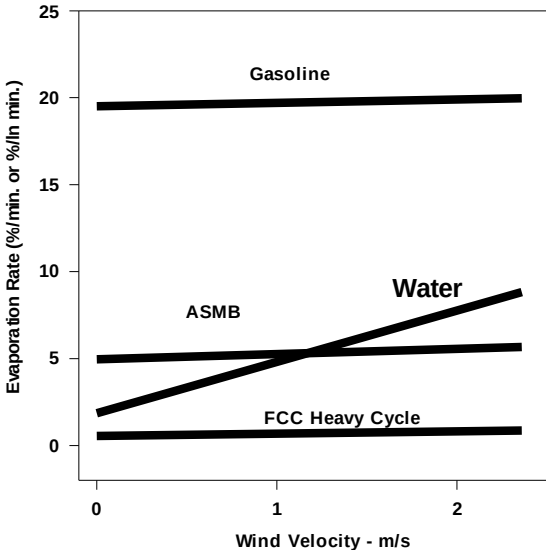

FIG. 4 CORRELATION OF EVAPORATION RATES AND WIND VELOCITY. THE LINES ARE DRAWN THROUGH THE DATA POINTS FROM EXPERIMENTAL VALUES. THIS CLEARLY SHOWS NO CORRELATION OF OIL EVAPORATION RATES WITH WIND VELOCITY AND THE STRONG AND EXPECTED HIGH CORRELATION OF WATER WITH WIND VELOCITY. THE WATER EVAPORATION LINE IS MOVED TO FIT ON THE VERTICAL SCALE, BUT OTHERWISE IS UNALTERED.

These experimental data show that oil is not air boundary-layer regulated. It should be noted that the air movement effect at the lowest level is a stirring effect which increases the diffusion of the components in the oil and thus the evaporation.

Saturation Concentration

An important concept of evaporation regulation is that of saturation concentration, the maximum concentration of a substance is soluble in air. The saturation concentrations of water and several oil components are listed in Table 1 showing that saturation concentration of water is less than that of common oil components (Fingas, 2011). The saturation concentration of water is in fact, about two orders of

magnitude less than the saturation concentration of volatile oil components such as pentane. This further explains why even light oil components have little boundary layer limitation.

Development of Generic Equations Using Distillation Data

The evaporation equations for oils show unique differences for oils under the same conditions, implying that unique equations may be needed for each oil and this fact is a significant disadvantage to practical end use. A method to accurately predict evaporation by means of other readily-available data is necessary (Fingas 1999). Findings show that distillation data can be used to predict evaporation. Distillation data are very common and often the only data used to characterize oils. This is because the data are crucial to operating refineries. Crude oils are sometimes priced on the basis of their distillation data.

Table 1 Saturation Concentration of Water and Hydrocarbons

Substance	Saturation Concentration * in g/m^3 at 25^{o}C
water	**20**
n-pentane	1689
hexane	564
cyclohexane	357
benzene	319
n-heptane	196
methylcyclohexane	192
toluene	110
ethybenzene	40
p-xylene	38
m-xylene	35
o-xylene	29

*Values taken from Ullmann's Encyclopedia

Oils and diesel-like fuels evaporate as two distinct types, those that evaporate as a logarithm of time and those that evaporate as a square root of time.[1] Most oils typically evaporated as a logarithm (natural) with time. Diesel fuel and similar oils, such as jet fuel, kerosene and the like, evaporate as a square root of time. The reasons for this are simply that diesel fuel and such like have a narrower range of compounds which evaporating at similar rates, yield rates which together sum as a square root.

The empirically measured parameters at 15^{o}C were correlated with both the slopes and the intercepts of the temperature equations. Full details of this correlation are given in the literature (Fingas 2011). For most oils and petroleum products, the variation with temperature resulting equation is:

$$\text{Percentage evaporated} = [B + 0.045(T-15)]\ln(t) \quad (33)$$

where B is the equation parameter at 15^{o}C, T is temperature in degrees Celsius and t is the time in minutes.

Distillation data were correlated to the evaporation rates determined by experimentation. The optimal point was found to be 180^{o}C by using peak functions. The percent mass distilled at 180 degrees was used to calculate the relationship between the distillation values and the equation parameters. The equations used were derived from correlations of the data. The data from those oils that were better fitted with square root equations - diesel, Bunker C light and FCC Heavy Cycle-were calculated separately. The equations derived from the regressions are as follows:

For most oils that follow a logarithmic equation:

$$\text{Percentage evaporated} = 0.165(\%D)\ln(t) \quad (34)$$

For oils that follow a square root equation such as diesel fuel:

$$\text{Percentage evaporated} = 0.0254(\%D)\sqrt{t} \quad (35)$$

where %D is the percentage (by weight) distilled at 180^{o}C. These equations can be combined with the equations generated in previous work to account for the temperature variations (Fingas 2011):

For oils (most oils and petroleum products) that follow a logarithmic equation:

$$\text{Percentage evaporated} = [.165(\%D) + .045(T-15)]\ln(t) \quad (36)$$

For oils like diesel fuel that follow a square root equation:

$$\text{Percentage evaporated} = [.0254(\%D) + .01(T-15)]\sqrt{t} \quad (37)$$

where %D is the percentage (by weight) distilled at 180^{o}C.

A large number of experiments were performed on oils to directly measure their evaporation curves. Examples of empirical equations obtained are given in Table 2.

Complexities to the Diffusion-Rgulated Model

Oil Thickness

Studies show that under diffusion regulation very thick slicks (much more than about 2 mm) evaporate slower than other slicks (Fingas 2011). This is due to the increased path length that volatile components must diffuse in a thicker slick. This can certainly be

confused with air-boundary-layer regulation. Experiments by the present author studied the effect of thickness on the evaporation of a light crude oil, Alberta Sweet Mixed Blend (ASMB) crude oil. The equations noted in Table 2 were all measured at a slick thickness of 1.5 mm which is typical of actual at sea values (Fingas 2011). The best curve fit is a square root function from which a correction can be given for thickness.

Corrected equation factor = equation factor +1 - 0.78 *√t (38)

Where the corrected equation factor is the factor corrected for the appropriate slick thickness, the logarithmic equation factor is that noted in Table 2, and t is the slick thickness in mm. This equation is true for thickness values above 1.5 mm at which the original equations were measured.

The Bottle Effect

Another confusing phenomenon to understanding evaporation is the bottle effect. If all the evaporating oil mass is not exposed, such as in a bottle, more oil vapors than those can readily diffuse through the air layer at the bottle mouth may yield a partial or temporary air-boundary-layer regulation effect which may end when the evaporation rate of the oil mass is lower than the rate at which the vapors can readily diffuse through the opening. Such effects could occur in reality in situations such as oil under ice, partially exposed to air or when a thick skin forms over parts of the oil, blocking evaporation.

Jumps from the 0-wind Values

Experimentation shows that studies of oil evaporation at no turbulence or air flow indicate a slight decrease in evaporation rate from those experiments carried out with slight air movement such as found in an ordinary room.[22] This is due to the slight stirring of the oil mass which increases the diffusion rate somewhat. Tests of this phenomenon indicate that further increases in evaporation rate do not occur with increased air movement or turbulence, thus confirming that this is a phenomenon only at 0-wind or turbulence conditions.

Use and Comparison of Evaporation Equations in Spill Models

Evaporation equations are the prime physical change equations used in spill models. A review of the use of evaporation algorithms in oil spill models is given in Fingas, 2011. This is because evaporation is often the most significant change that occurs in an oil's composition. Many models in the decade after 1984 use the Stiver and Mackay (1984) approach. Currently, more models employ equations such as found in Table 2.

Table 2 Sample of Empirical Equations of Oil Evaporation

Oil Type	Equation
Alaska North Slope	%Ev = (2.86 + .045T)ln(t)
Alberta Sweet Mixed Blend	%Ev = (3.24 + .054T)ln(t)
Arabian Medium	%Ev = (1.89 + .045T)ln(t)
Arabian Heavy	%Ev = (2.71 + .045T)ln(t)
Arabian Light	%Ev = (3.41 + .045T)ln(t)
Barrow Island, Australia	%Ev = (4.67 + .045T)ln(t)
Boscan, Venezuela	%Ev = (-0.15 + .013T)/t
Brent, United Kingdom	%Ev = (3.39 + .048T)ln(t)
Bunker C - Light (IFO~250)	%Ev = (.0035 + .0026T)/t
Bunker C - long term	%Ev = (-.21 + .045T)ln(t)
Bunker C (short term)	%Ev = (.35 + .013T)/t
California API 11	%Ev = (-0.13 + .013T)/t
Cano Limon, Colombia	%Ev = (1.71 + .045T)ln(t)
Chavyo, Russia	%Ev = (3.52 + .045T)ln(t)
Cold Lake Bitumen, AB Canada	%Ev = (-0.16 + .013T)/t
Delta West Block 97, USA	%Ev = (6.57 + .045T)ln(t)
Diesel - long term	%Ev = (5.8 + .045T)ln(t)
Diesel Fuel short term	%Ev = (0.39 + .013T)/t
Ekofisk, Norway	%Ev = (4.92 + .045T)ln(t)
Federated, AB, Canada	%Ev = (3.47 + .045T)ln(t)
Fuel Oil #5	%Ev = (-0.14 + .013T)/t
Gasoline	%Ev = (13.2 + .21T)ln(t)
Gulfaks, Norway	%Ev = (2.29 + .034T)ln(t)
Hout, Kuwait	%Ev = (2.29 + .045T)ln(t)
IFO-180	%Ev = (-0.12 + .013T)/t
Isthmus, Mexico	%Ev = (2.48 + .045T)ln(t)
Jet A1	%Ev = (.59 + .013T)/t
Komineft, Russian	%Ev = (2.73 + .045T)ln(t)
Lago, Angola	%Ev = (1.13 + .045T)ln(t)
Lago Treco, Venezuela	%Ev = (1.12 + .045T)ln(t)
Maya, Mexico	%Ev = (1.38 + .045T)ln(t)
Nugini, New Guinea	%Ev = (1.64 + .045T)ln(t)
Sahara Blend, Algeria	%Ev = (0.001 + .013T)/t
Sakalin, Russia	%Ev = (4.16 + .045T)ln(t)
Scotia Light	%Ev = (6.87 + .045T)ln(t)
South Louisiana	%Ev = (2.39 + .045T)ln(t)
Statfjord, Norway	%Ev = (2.67 + .06T)ln(t)
Taching, China	%Ev = (-0.11 + .013T)/t
Troll, Norway	%Ev = (2.26 + .045T)ln(t)
Udang, Indonesia	%Ev = (-0.14 + .013T)/t
West Texas Intermediate	%Ev = (2.77 + .045T)ln(t)
West Texas Sour	%Ev = (2.57 + .045T)ln(t)

The comparison of air-boundary-layer models with

the empirical equations leads to some interesting conclusions on their applicability. Figure 5 shows a comparison of the prediction of evaporation of diesel fuel using an air-layer-boundary model and an empirical curve. The 0-wind diesel evaporation calculated using an air-layer-boundary model comes closest to the empirical curve, however, prediction is of the wrong curvature. The prediction of diesel evaporation using the wind levels shown, results in prediction errors as great as 100 percent over about 200 hours. Figure 6 shows a comparison of the evaporation of Bunker C using two air-layer-boundary models and an empirical curve. The 0-wind evaporation air-boundary-layer prediction comes closest to the empirical curve. As most comparisons shown, the evaporation rate up to about 8 hours is similar to the empirical curve. The prediction of Bunker C evaporation using the wind levels shown results in prediction errors as great as 400 percent over about 200 hours (direct differential in percentage differences). These high values of Bunker C evaporation as predicted by air-boundary-layer models with wind conditions are completely impossible, as shown by extensive experimentation and field measurements.

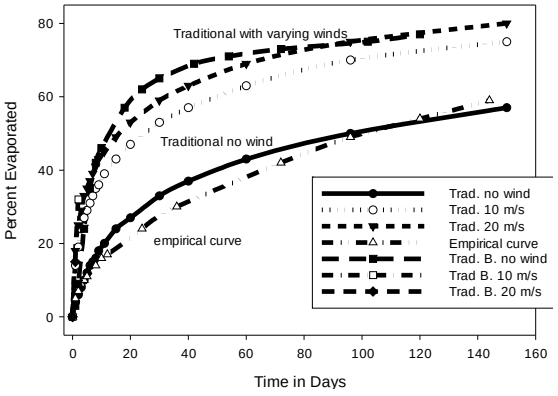

FIGURE 5 A COMPARISON OF THE EVAPORATION OF DIESEL FUEL USING AN AIR-LAYER-BOUNDARY MODEL (SUCH AS FROM EQUATION (30) AND AN EMPIRICAL CURVE SUCH AS FROM TABLE 2.

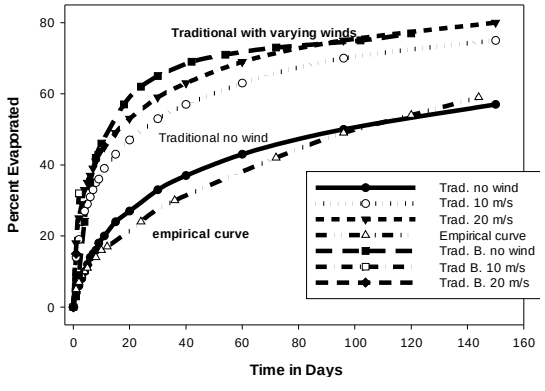

FIG 6 A COMPARISON OF THE EVAPORATION OF BUNKER C USING TWO AIR-LAYER-BOUNDARY MODELS (SUCH AS FROM EQUATION 30) AND AN EMPIRICAL CURVE (FROM TABLE 2).

The 0-wind diesel evaporation calculated using an air-layer-boundary model comes closest to the empirical curve, however, is of the wrong curvature. The prediction of diesel evaporation using the wind levels shows errors as great as 100 percent over about 200 hours.

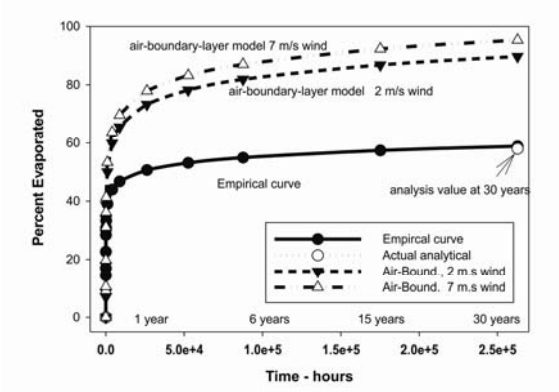

FIG 7 A COMPARISON OF THE EVAPORATION OF PEMBINA CRUDE USING AN AIR-LAYER-BOUNDARY MODEL (EQUATION 30), AN ACTUAL ANALYSIS AFTER 30 YEARS AND AN EMPIRICAL CURVE. THE EVAPORATION RATE UP TO ABOUT 100 HOURS IS SIMILAR TO THE EMPIRICAL CURVE. THE PREDICTION OF LONG-TERM EVAPORATION USING EVEN SMALL WIND LEVELS SHOWN RESULTS IN PREDICTION ERRORS AS GREAT AS 60 PERCENT OVER ABOUT 10 YEARS. THESE HIGH VALUES OF EVAPORATION AS PREDICTED BY AIR-BOUNDARY-LAYER MODELS WITH WIND CONDITIONS ARE NOT REALISTIC.

The 0-wind evaporation prediction comes closest to the empirical curve. The prediction of Bunker C evaporation using the wind levels shown results in prediction errors as great as 400 percent over about 200 hours. These high values of Bunker C evaporation as predicted by air-boundary-layer models with wind conditions are completely impossible. As most comparisons shown, the evaporation rate calculated by most means up to about 10 hours is similar to the empirical curve.

Thus there are three major errors resulting from the use of air-boundary-layer models, and the first and most important is that they cannot accurately deal with long term evaporation; then, the wind factor results in unrealistic values and finally, they have not been adjusted for the different curvature for diesel-like evaporation. Some modelers have adjusted their models using air-boundary-layer models to avoid very high values at long evaporation times by setting a maximum evaporation value, which works after a point in time, but does so artificially. Most models of any type will require that one sets a maximum rate to avoid over prediction or values over 100%, for

example. This can be best illustrated using a long term example. A spill in northern Alberta of Pembina oil was sampled 30 years after its spill. Analysis shows that this was weathered to the extent of 58% (Wang et al. 2004). Figure 7 shows the comparison of the actual value, the empirical projection and the air-boundary-layer predicted value, indicating that the air-boundary-predicted value overshoots the estimate by over 60%, despite the use of only two low wind values of 2 and 7 m/s. Use of higher wind values increases the evaporation to well over 100%.

Conclusions

A review of oil evaporation shows that oil evaporation is not air-boundary-layer regulated. The results of several experimental series have shown the lack of air boundary-layer regulation. The fact that oil evaporation is not strictly boundary-layer regulated implies that a simplistic evaporation equation will suffice to describe the process. The following factors do not require consideration: wind velocity, turbulence level, area, and scale size. The factors significant to evaporation include time and temperature.

A comparison of the various models used for oil spill evaporation shows that air-boundary-layer models result in erroneous predictions. There are three issues including that air-boundary-layer models cannot accurately deal with long term evaporation; second, the wind factor results in unrealistic values and finally, they have not been adjusted for the different curvature for diesel-like evaporation. There has been some effort made on the part of modellers to adjust air-boundary-layer models to be more realistic for longer-term evaporation but these may be artificial and result in other errors such as under-estimation for long-term prediction.

A diffusion-regulated model has been presented along with many empirically-developed equations for many oils. The equations are found to be of the form shown in equation (34)

It is also noted that in terms of diesel fuel and similar oils the curve is different and follows a square root curve as predicted by equation (35).

The most accurate predictions are carried out using the empirical equations as noted in Table 2. If these are not available, the parameters can be estimated using distillation data as shown by equations (36) and (37).

Marine environments are complex, with many difference from controlled experiments. It is therefor important to have models that correspond closely to the actual physics to begin to more accurately model phenomena such as evaporation.

REFERENCES

Blokker, P.C., "Spreading and Evaporation of Petroleum Products on Water", in *Proceedings of the Fourth International Harbour Conference*, Antwerp, Belgium, pp. 911-919, 1964.

Bobra, M., *A Study of the Evaporation of Petroleum Oils*, Manuscript Report Number EE-135, Environment Canada, Ottawa, ON., 1992.

Brighton, P.W.M., "Evaporation from a Plane Liquid Surface into a Turbulent Boundary Layer", *Journal of Fluid Mechanics*, Vol. 159, pp 323-345, 1985.

Brighton, P.W.M., "Further Verification of a Theory For Mass and Heat Transfer From Evaporating Pools", *Journal of Hazardous Materials*, Vol. 23, pp. 215-234, 1990.

Brutsaert, W., *Evaporation into the Atmosphere*, Reidel Publishing Company, Dordrecht, Holland, 299 p., 1982.

Butler, J.N., "Transfer of Petroleum Residues from Sea to Air: Evaporative Weathering", in *Marine Pollutant Transfer*, Ed H.L. Windom and R.A. Duce, Lexington Books, Toronto, pp. 201-212, 1976.

Drivas, P.J., "Calculation of Evaporative Emissions from Multicomponent Liquid Spills", *Environmental Science and Technology*, Vol. 16, pp. 726-728, 1982.

Fingas, M., "Evaporation Modeling", Chapter 9, in *Oil Spill Science and Technology*, M. Fingas, Editor, Gulf Publishing, NY, NY, pp. 201-242, 2011.

Fingas, M.F., "A Literature Review of the Physics and Predictive Modelling of Oil Spill Evaporation", *Journal of Hazardous Materials*, *Vol. 42*, pp.157-175, 1995.

Fingas, M.F., "Studies on the Evaporation of Crude Oil and Petroleum Products: I. The Relationship between Evaporation Rate and Time", *Journal of Hazardous Materials*, *Vol. 56*, pp. 227-236, 1997.

Fingas, M.F., "Studies on the Evaporation of Crude Oil and Petroleum Products: II. Boundary Layer Regulation", *Journal of Hazardous Materials*, *Vol. 57*, pp. 41-58, 1998.

Fingas, M.F., "The Evaporation of Oil Spills: Development and Implementation of New Prediction Methodology", in *Proceedings of The 1999 International Oil Spill Conference*,

American Petroleum Institute, Washington, D.C., pp. 281-287, 1999.

Goodwin, S.R., D. Mackay and W.Y. Shiu, "Characterization of the Evaporation Rates of Complex Hydrocarbon Mixtures under Environmental Conditions", *Canadian Journal of Chemical Engineering*, Vol. 54, pp. 290-294, 1976.

Hamoda, M.F., S.E.M. Hamam and H.I. Shaban, "Volatization of Crude Oil from Saline Water", *Oil and Chemical Pollution*, Vol. 5, pp. 321-331, 1989.

Jones, F.E., *Evaporation of Water*, Lewis Publishers, Chelsea, Michigan, 188 p., 1992.

Li Y.Y., X.L. Zheng, B. Li, Y.X. Ma and J.H. Cao, "Volatilization Behaviors of Diesel Oil from the Soils", *Journal of Environmental Science* (China), pp. 1033-1038, 2004.

Mackay, D. and R.S. Matsugu, "Evaporation Rates of Liquid Hydrocarbon Spills on Land and Water", *Canadian Journal Chemical Engineering*, Vol. 51, Canadian Society for Chemical Engineering, Ottawa, Ontario, pp 434-439, 1973.

Monteith, J.L. and M.H. Unsworth, *Principles of Environmental Physics*, Hodder and Stoughton, 2008.

Quinn, M.F., K. Marron, B. Patel, R. Abu-Tanbanja and H. Al-Bahrani, "Modelling of the Ageing of Crude Oils", *Oil and Chemical Pollution*, Vol. 7, pp. 119-128, 1990.

Reijnhart, R. and R. Rose, "Evaporation of Crude Oil at Sea", *Water Research*, Vol. 16, pp. 1319-1325, 1982.

Stiver, W. and D. Mackay, "Evaporation Rate of Spills of Hydrocarbons and Petroleum Mixtures", *Environmental Science and Technology*, Vol. 18, pp. 834-840, 1984.

Sutton, O.G., "Wind Structure and Evaporation in a Turbulent Atmosphere", *Proceedings of the Royal Society of London, A 146*, pp. 701-722, 1934.

Technology, Vol. 16, pp. 726-728, 1982.

Tkalin, A.V., "Evaporation of Petroleum Hydrocarbons from Films on a Smooth Sea Surface", *Oceanology of the Academy of Sciences of the USSR*, Vol. 26, pp 473-474, 1986.

Wang, Z., M. Fingas, C. Yang, B. Hollebone, and X. Peng, "Biomarker Fingerprinting: Applications and Limitations for Source Identification and Correlation of Oils and Petroleum Products", in Proceedings of the Twenty-Seventh Arctic and Marine Oil Spill Program Technical Seminar, Environment Canada, Ottawa, Ontario, pp. 103-124, 2004.

Yang, W.C. and H. Wang, "Modelling of Oil Evaporation in Aqueous Environment", *Water Research*, Vol. 11, pp. 879-887, 1977.

Merv F. Fingas A scientist in Edmonton, Alberta, Canada, Dr. Fingas has a PhD in environmental physics from McGill University (1996), three masters degrees; chemistry (1984), business and mathematics (1978), all from University of Ottawa. He also has a bachelor of science in Chemistry from Alberta (1974) and a bachelor of arts from Indiana (1968).

He was Chief of the Emergencies Science Division of Environment Canada for over 30 years in Ottawa, Ontario and is currently work on research in Edmonton, Western Canada. He works here as an independent researcher and he has published more than 800 papers and publications in the field in addition to 7 books prepared on spill topics and working on 2 others.

Dr. Fingas is a member of the American Chemical Society and the American Association for the Advancement of Science. He has been active in the American Society for Testing and Materials and awarded the honor of 'fellow' of this society.

Current Overview of Cyclic Steam Injection Process

Johannes Alvarez*[1], Sungyun Han*[2]

*Co-first authors are listed in alphabetical order.

[1,2] Texas A&M University, Department of Petroleum Engineering, College Station, Texas, 77843, USA

[1] johannes.alvarez@pe.tamu.edu; [2]sungyun.han@pe.tamu.edu

Abstract

Cyclic Steam Injection (CSI) is an effective thermal recovery process, in which, several driving mechanisms define the success of the process; i.e. viscosity reduction, wettability alteration, gas expansion, etc. This process was first applied in late 1950s. Then, it has been applied world-wide successfully to both light and heavy oil reservoirs. To increase the effectiveness of CSI, process was varied by chemical addition to steam, application of horizontal wells and introduction of hydraulic fracturing. With these modern technologies, average 15% of recovery factor of conventional CSI producers back in 1980's boosted up to approximately 40%. The method is attractive because it gives quick payout at relatively high success rate due to cumulative field development experiences. However, this is still uncompetitive in terms of ultimate recovery factor compared to that of other steam drive methods such as steam flooding (50-60% OOIP) or SAGD (60-70% OOIP).

Recent studies related to the CSI have focused on either the optimization of chemical additives and fracture design or questioning on geomechanical solutions to poroelastic effects. In addition, most papers discuss about follow-up process posterior to CSI such as in-situ combustion, CO_2 injection and steam flooding. This study is oriented to overview of the past and current status of CSI process in technical aspects with discussion of commercial cases throughout the world. A summarized review is given on the potential importance of encouragement of further investigation of Cyclic Steam Injection.

Keywords

Cyclic Steam Injection; Cyclic Steam Stimulation; Huff n' Puff; Thermal Enhanced Oil Recovery

Introduction

Cyclic Steam Injection, also called Huff n' Puff, is a thermal recovery method which involves periodical injection of steam with purpose of heating the reservoir near wellbore, in which, one well is used as both injector and producer, and a cycle consisting of 3 stages, injection, soaking and production, repeats to enhance the oil production rate as shown in Fig. 1. Steam is injected into the well for certain period of time to heat the oil in the surrounding reservoir to a temperature at which it flows (200~300°C under 1 MPa of injection pressure). When enough amount of steam has been injected, the well is shut down and the steam is left to soak for some time no more than few days. This stage is called soaking stage. The reservoir is heated by steam, consequently oil viscosity decreases. The well is opened and production stage is triggered by natural flow at first and then by artificial lift. The reservoir temperature reverts to the level at which oil flow rate reduces. Then, another cycle is repeated until the production reaches an economically determined level.

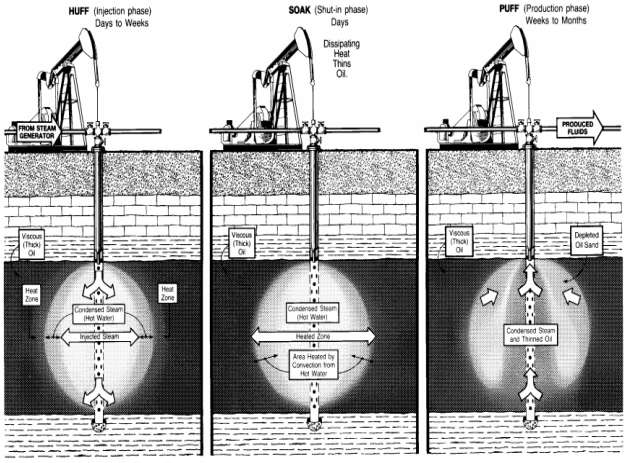

FIG. 1 CYCLIC STEAM INEJCTINO PROCESS (FROM UNITED STATES DEPARTMENT OF ENERGY, WASHINGTON DC.)

Typical CSI process is well suited for the formation thickness greater than 30 ft and depth of reservoir less than 3000 ft with high porosity (>0.3) and oil saturation greater than 40%. Near-wellbore geology is critical in CSI for steam distribution as well as capture of the mobilized oil. Unconsolidated sand with low clay content is favorable. Above 10 API gravity and viscosity of oil between 1000 to 4000 cp is considerable while permeability should be at least 100 md (Thomas, 2008; and Speight, 2007).

Underlying Technology

CSI includes three stages; injection, soaking and production, which are repeated until the oil production turns uneconomic (Prats, 1985, and Thomas, 2008). Application of CSI, like other EOR methods, targets to reduce the formation residual oil saturation by several driving mechanisms: viscosity reduction, changes in wettability and thermal and solution gas expansion (Prats, 1978) which depend on reservoir rock and fluid properties. For instance, viscosity reduction can be explained by mobility ratio which is the ratio of effective permeability to viscosity.

In addition, during CSI many chemical reactions occur which mainly form gaseous components such as carbon dioxide, hydrogen sulfide, and hydrogen during steam injection (Hongfu et al., 2002); and these reactions include decarboxylation of the crude, formation of H_2S from sulfur in the crude, formation of H_2, CO, CH_4 and CO_2 from reactions between water and crude and formation of CO_2 by decomposition and reactions of carbonates minerals (Prats, 1985).

The produced gases formed during the CSI create additional driving mechanism which can be named as gas drive. Also, these visbreaking reactions reduce the oil viscosity by increasing the oil mobility (Pahlavan et al., 1995, Hongfu et al., 2002, and Prats, 1985). Hongfu et al., in 2002 reported a reduction of heavy oil viscosity between 28 and 42% after CSI.

Reservoir Properties Changes with CSI

Every stimulation that is performed in the reservoir has consequences; introducing heat into the formation by CSI produces stress and deformation in oil sand formations. The resulting pore volume changes affect the reservoir permeability and consequently water mobility. Scott et al., in 1994, claimed that the volume and permeability changes are the results of three effects: change in the mean principal effective stress, change in the shear stress and change in temperature. The increase in temperature causes thermal expansion of the sand grains and sand structure. In addition, studies conducted in Cold Lake field in Canada concluded that, during steam injection, the increase of pore pressure decreases the effective confining stress and causes an unloading of the reservoir (Scott et al., 1994).

In the Clearwater formation in Canada, the effects of the volumetric expansion, during CSI, were transferred to the reservoir surrounding and the surface (Walters et al., 2000). This is sometimes observed as small elevations of the surface near the well, usually in shallow reservoirs. In addition, Walters et al., 2002 explained pressure changes in an isolated aquifer overlying the Clearwater formation as the result of poroelastic effects during CSI. However, these geomechanical deformations and failure mechanisms produced by CSI give the initial injectivity required for steam injection and the drive energy needed for the oil production (Yuan et al., 2011).

CSI, due to the injection of a hot fluid into the formation, causes shear dilation (Wong et al., 2001). Hence, the pore rock characteristics change by means of enlarging their volume. This increases permeability which affects directly steam and hydrocarbon movements in the reservoir. Wong et al.. developed a model that provided a quantitative estimation of the permeability changes caused by shear dilation.

Yale et al. affirmed that the most significant impact of dilation due to CSI is an increase in the permeability to water. This increase of the pore space is caused dilatation and mobility of the injected fluid. Further, condensation of hot water from steam ahead of the steam front pressurized the reservoir (Yale et al., 2010). Moreover, CSI induced displacements in the reservoir due to dilation and the recovery of these original conditions during production operations is a point of supply of reservoir drive energy.

Gronseth, in 1989, studied the distribution of the injected fluids during CSI in the Clearwater formation, and found that if the injection rates are faster than diffusion rates into the matrix, the reservoir volume increases to adjust the volume of the injected fluid. This volume increase is translated into a pressure increase. Later, during production, reservoir pressure reduces and effective stresses increases, so the reservoir contracts and a portion, but not the entire increased reservoir volume, is recovered (Gronseth, 1989).

There are techniques used to monitor reservoir deformation. These measures are important to optimize production and design parameters such as well length, well spacing, injection rate, cycle time, among others. In CSI, inclinometers and tilt-meters, based on surface deformation, are used to monitor steam migration and formation dilation (Du et al., 2005). However, tilt-meters are more accurate than inclinometers by more than one order of magnitude (Dusseault et al., 2002).

History: Commercial Cases

CSI was first used fortuitously in Venezuela in 1959. By that time, one of the steam injector wells began to produce, after a blowout, in much better conditions than the surrounding production wells (Trebolle and Chalot, 1993). Since then, this method has been applied in many fields such as Bolivar Coastal and Santa Barbara in Venezuela (Valera et al., 1999), Cold Lake Oil Sands in Canada, Xinjiang and Liaohe in China (Liguo et al., 2012), Midway-sunset in California (Jones et al., 1990), among other heavy oil fields.

At the early stages of CSI application, CSI was considered as an old-school oil production method in which operations are ahead of research developments (Ramey et al., 1969). The literature shows that many publications, explaining CSI processes, were based on field experiences rather than research work. There are a lot of unknowns about the process parameters such as the number of stimulation cycles, well orientation and number of wells, operating condition, the increase of water cut, among others. Therefore, on early CSI field applications, the process was performed as trial-and-error field-scale experiment (Ramey, 1967). After many research studies and field experiences, important technology problems were reduced.

First, the number of stimulation cycles increased by time. By 1974, CSI has an average of three stimulation cycles with a maximum reported of 22 (Ali et al., 1974). In 1990, in the Midway-Sunset field, California, there was already a well with 39 cycles. Also, out of 1500 wells, there were 75 wells with more than 30 cycles, and 350 wells with more than 20 cycles (Jones et al., 1990). This increment in the number of cycles was accomplished by getting better understanding of steam properties, reservoir characteristics, and injection conditions.

Second, well orientation and number of wells were improving by time. In Trinidad and Tobago, slim-hole injectors, insulated tubing and packers, and limited entry perforations have been used to combat gravity segregation consequences (Khan, 1992). As well, steam was injected with foam-diverting agents to control water breakthrough resulting from high injectivity.

In addition, in the Cold Lake oil sands, Canada, steam distribution in horizontal wells was improved by using screen sections, which facilitated contact between the well and the reservoir. Also, inside these screen sections, small flow orifices were used to control the flow between the inner pipe and the reservoir to enhance oil production and reduce steam consumption (Oil and Gas Journal report by Bob Tippee, 2012).

In China, the most up to date methods and techniques used in CSI include: high-efficient steam injection by automatic controlling steam generation, insulating surface pipeline and multi-zone steam injection; as well as artificial lifting, sand control, CSI with chemical additives, re-entry drilling technology, and process control systems (Haiyan et al., 2005). In addition, steam distribution has been improved by using separated-zone steam injection techniques such as selected, dual and multi zone injection, either sequentially or simultaneously. This method showed, in field testing to 76 wells of the Liaohe oil field, an increase up to 70% of the steam zone (Liguo et al., 2012). Moreover, as well in horizontal well, the tubing and annulus of the same well have been applied to inject to in the toe and heel separately (Liguo et al., 2012).

Third, operating conditions of pressure and temperature have adjusted to each case based on reservoir properties and well design. In the Cold Lake field, CSI has been achieved by injection at pressures high enough to fracture the formation (Beattie et al., 1991). In California, specifically in Potter sands in the Midway-Sunset field, a sequential steaming process was implemented. This approach involved heating the reservoir rather than heating each well separately (Jones et al., 1990). The wells were stimulated in rows from down to up dip of the reservoir. Using this methodology, the production per well increased up to a rate of 30% per year (Jones et al., 1990).

Another technique, in pilot stage and successfully simulated, is the use of Top-Injection Bottom-Production (TINBOP) whose principle is to inject steam at the top of the reservoir using the short well string and produced from the bottom of the reservoir using the long well string. (Morlot et al., 2007). Simulation studies, conducted by Morlot et al. showed TINBOP increased oil recovery by 57 to 93%, compared to conventional CSI (Morlot et al., 2007). One feature of this method is that there is no soaking period.

Fourth, the increase of water cut is also addressed. In CSI, each succeeding cycle normally increases water cuts (Ali et al., 1974). Consequently, in the late 70's there was a trend to convert these operations into

steam drives due to the decrement in oil recovery (Prats, 1978). This trend has changed in the last years with the use of chemical additives on CSI.

Recently, there have been important progresses in oil recovery using chemical addition. Although CSI increases oil recovery, chemical addition with CSI increases it even further (Ramey et al., 1967). Nowadays, in CSI processes, co-injection of steam with gels, foams, and surfactants, among other chemicals, are used to increase oil production and reduce water production. In Russia, specifically in the Permian-Carboniferous reservoirs of the Usinsk field, gels and foams have been injected with CSI from 2007 to 2011, and an increase of 20-30% oil rate and decreased 33-35% water cut (Taraskin et al., 2012) have been observed.

In Canada, Liquid Addition to Steam for Enhancing Recovery (LASER) has been field-tested for a single cycle at Cold Lake field. Previous work indicated that, if successful, the LASER process could increase the recovery factor by 3 – 6% OOIP (Leaute et al., 2007).

Similarly in Canada, other processes have been tested to increase CSI performance such as air injection, achieving 15% incremental in addition to the 12-20% recovery with high pressure CSI (Jiang et al., 2010), and biodiesel and carbamide injection (Babadagli et al., 2010 and Zhang et al., 2009), both used as surfactants to enhance the CSI efficiency.

The field tests in Henan Oil Field, China, using carbamide increased oil recovery by 7% and decreased Residual Oil Saturation (SOR) almost by 1% (Zhang et al., 2009). As well, in the Bachaquero field in Venezuela, an ionic-alkyl-aryl sulfonate surfactant (LAAS) has been used to generate foams that enhance steam distribution more evenly in the reservoir by restricting steam to the areas with higher permeability. This technique has improved the production per cycle from 15 to 40% (Valera et al., 1999). Moreover, solvents have been used to improve steam injectivity by removing organic deposits from the rock and changing its wettability in Costa Bolivar, Zulia, Venezuela (Mendez et al., 1992).

Finally, wettability changes in CSI due to temperature increase have been studied by several authors with different results. On one hand, there is a line of thought which assures that as temperature increases, the system oil-water-rock becomes more water-wet (Prats, 1985, Schembre et al., 2006, Kovscek et al., 2008, and Poston et al., 1970). On the other hand, another tendency advocates that the system becomes more oil-wet as temperature increases (Rao and Karyampudi, 1999, Escrochi et al., 2008, and Rao, 1999); also, there is a third line of thought explaining that wettability is independent of temperature changes (Miller and Ramey, 1985, and Pollkar et al., 1989).

Studies with Diatomaceous rocks and Berea sandstones conducted by Schembre et al., 2006, showed that both diatomaceous and Berea cores become more water-wet as temperature increases (from 100 to 200°C). This behavior was attributed to fines detachment, in low salinity and high pH steam condensate fluid, which stabilizes a thin water film that covers the rock surface avoiding contact with the oil phase. This fines detachment depends on temperature and mineralogy; for example, wettability changes are reached faster in silica than that in clays (Schembre et al., 2006). In addition, Poston et al., 1970, conducted similar studies using unconsolidated sands from Houston sands and Midway-Sunset field, California, reaching the conclusion that increasing temperature (from 25 to 150°C) is determined in improving water-wetness in the unconsolidated sands.

On the other hand, Rao and Karyampudi, 1999, and Rao, 1999, conducted CSI lab and field test in the heavy oil and bitumen Elk Point Cummings formation, Canada. Their results showed that at high temperatures (162 to 196–°C), the formation, which is mainly silica (87%), became oil-wet. Moreover, they also discover that salt deposition, mainly calcium carbonate ($CaCO_3$), in one of the core layers prevented oil-wet behavior at high temperatures, changing the wettability to water-wet. This effect was proved in core flooding and field test in which increment in oil rate and decrement in water cut were observed (from 22 BPD and 83% in the fourth cycle to 51 BPD and 77% in the five cycle) (Rao and Karyampudi, 1999).

Wettability reversal effect at high temperatures is also attributed to asphaltene precipitation. Using Athabasca bitumen and live oil sample with 5% and 3.17% asphaltene respectively, Escrochi et al., 2008, showed that from 150 to 400 °C the system shifted to oil-wet until asphaltene precipitation was completed and then wettability was changed to water-wet.

Moreover, in the literature, results showed that temperature do not impact wettability during CSI, and Miller and Ramey, 1985 tested the unconsolidated Ottawa Silica Sand and a consolidated Berea Sandstone with temperatures from 25 to 150° C, concluding that there were not changes in residual

saturations that imply variance in wettability. The same results were reached in the unconsolidated silica sands at 125 to 175 °C by Pollkar et al., 1989.

Consequently, when CSI is applied, there are different positions in describing wettability mechanism and their changes with temperature. However, it is important to point out that these results mainly depend on the chemical properties of fluids injected, asphaltene content and the mineralogy of the reservoir.

From its early stages until today, CSI has evolved significantly from a process discovered by chance where trial and error governed the operations with little number of cycles and low recovery factor to state-of-the-art applications with a great variety of chemical additives and well geometries which increase the number of cycles and the ultimate oil recovery. However, more research needs to be done in evaluating wettability changes at field scale to determine the factors that influence early water break and reduce oil production at different mineralogy and injection temperatures.

Current State-of-the-art: Applications

The method is quite effective, especially in the first few cycles providing quick payout. However, ultimate recovery by cyclic steam injection is low (10-40% of Original Oil in Place, OOIP), compared to that of steam flooding and Steam Assisted Gravity Drainage (SAGD) which are over 50% of OOIP (Thomas, 2008; Speight, 2007; Xia and Greaves, 2006) as shown in TABLE. 1. Therefore, it is quite common for wells to be produced in the cyclic steam manner for a few cycles before put on a steam flooding regime with other wells (Alikhlalov et al., 2011).

TABLE 1 OIL RECOVERY RATE OF THERMAL EOR METHODS

Oil Recovery Factors (successful projects)	
Thermal EOR	% of OOIP
CSI	10 - 40
Steam flooding	50 - 60
SAGD	60 - 70
In-situ Combustion*	70 - 80

*In-situ Combustion using THAI—'Toe-to-Heel Air Injection'

Conventional CSI process usually has average recovery factor lower than 20%. However, this can be doubled with combination of unconventional technologies which have become profitable including co-injection of steam with chemical additives, directional drilling, and hydraulic fracturing. Recently, technical aspects like injected steam/produced oil ratio, presence of water cut in the producing well and excessive heat losses have required special attention. Many literatures have presented studies on these areas at laboratory scale (i.e, Castro et al., 2010). Investigations have been optimizing the cyclic steam injection technology by chemical addition to the steam. Currently, the performance of CSI is enhanced by co-injection of steam with chemicals such as surfactants, solvents, miscible and immiscible gases.

CSI with Chemical Additives

Since 1960, investigations on cyclic steam injection technology have been conducted to improve recovery factor by adding chemical additives to steam, fracturing, and placing horizontal wells for different types of reservoir. In the reservoir, the chemical additives enhance the production by increasing the mobility of oil and enabling condensed water to carry higher loading of oil. Numerous studies on chemical additives to steam have been conducted to affect heavy oil properties favorably such as solvents, surfactants, miscible and immiscible gases.

1) Solvents

The idea of adding solvents to the steam to reduce the oil viscosity has been reported in the literature since 1970s. Previously, solvents and light crudes had been used as diluents to optimize pumping and pipeline transportation of heavy crudes. Both laboratory and field tests later years proved that the use of solvent as an additive to steam during in-situ recovery improved the mobility ratio of displacing and displaced fluid and sweep efficiency. The mechanism is following: the vaporized solvent is co-injected with steam and travels with the steam front. It condenses and mixes with the oil in the cooler regions of reservoir creating a transition zone of lower-viscosity fluid between steam and oil. Consequently, the mobility ratio between steam and oil increases, resulting in higher production rate.

The success of process depends on the solvent type, treatment size and the solvent placement. It was concluded that the use of small quantities of medium volatile solvent (no more than 10% of steam volume) creates the best effectiveness in increasing total oil production (Shu and Hartman, 1988). In many of the previous researches, naphtha

was employed quite frequently which was found to be highly effective in opening a steam flow path due to its high volatility. Other solvents that were used in recent researches include CO_2, ethane, and a mixture of gases (Yongtao et al., 2011), kerosene, and even some effluents from some refinery processes (Castro et al., 2010).

2) Surfactants

Although adding solvents to steam can increase production recovery up to 30% upon earlier cycles, high injection volumes are required to reduce the viscosity of oil appreciably thereby necessitating solvent recovery, which leads to high operational costs. Therefore, adding surfactants to injected steam to reduce oil-water interfacial tension and alter wettability and therefore increase recovery was introduced. Most widely used agent is called Thin Film Spreading Agents (TFSA). TFSA compounds reduce interfacial tension by the application of a spreading film strong enough to overcome the emulsifying agents naturally found between the oil-water and oil-rock interfaces. By reduction of the interfacial energies between the oil-rock and water-rock, water wetting of the rock results, leading to the release of oil particles from the rock surface improving oil mobility (Adkins et al., 1983). Successful field applications of TFSA in California and Alberta were reported with indication of significant improvement in heavy oil recovery factor up to 20% (Srivastava and Castro, 2011).

The capability of the steam-surfactant mixture to divert steam entry into the sands varies directly with the concentration of the surfactant present, steam quality and the addition of a non-condensable gas. Some pilot tests in Bolivar Coast, Venezuela, reported the optimum level of surfactant concentration in the steam liquid phase 1 to 1.3 % (Robaina et al., 1988) above which no additional diversion was obtained. Most conventional surfactant injection projects, steam quality maintained averagely 60 to 70% (Blair et al 1982; Adkins et al., 1983). Co-injections of more efficient surfactants were also tested; however, they required high steam quality as 80 to 90%, which causes higher operating costs. Srivastava and Castro reported that TFSA requires only small amount of concentration (250 ppm) while sustaining steam quality as below 70% (Srivastava and Castro, 2011). Additionally, some laboratory tests demonstrated that introducing non-condensable gases (i.e nitrogen) helps to stabilize the foam, affording greater plugging of the porous media consequently (Robaina et al., 1988).

CSI with Horizontal Well

Due to the presence of certain sand volumes at the bottom of the reservoir which is not recoverable by using vertical wells, the idea of horizontal well was introduced to the CSI process. The main advantages of the horizontal wells are improved sweep efficiency, increased producible reserves as well as steam injectivity, and decreased number of well required for field development (Joshi, 1991). Although most of simulation studies proved notable advantages of horizontal well over vertical well (Adegbesan 1992, and Chang et al., 2009), CSI with horizontal well had little success in fields before 2000s. The main reason was the extra operating costs which were double that of vertical wells back then. Other factors include geological/reservoir characteristics and operational aspects such as uneven steam distribution and sand productions. For example, the activity of horizontal drilling in Bachaquero field in Venezuela where high oil viscosity (~18000 cp) encountered did not appear profitable, causing a low annular fluid level (Mendoza et al., 1997). A simulation study later on also showed that the application of horizontal well in same field was not economically attractive (Escobar et al., 2000).

On the other hand, few pilot tests in early 2000s had success on horizontal well application; and indeed, those horizontal producers in comparison to typical vertical ones in each area improved production performance and thermal efficiency as well as operating costs. Representative pilots are in South Midway-Sunset field (McKay et al., 2003) and Cymric/McKittric field in California (Cline et al., 2002). Both fields showed about 20 to 50% improvement in production over results from vertical wells and benefited from maximum 45% of directional drilling cost reduction relative to that of a decade ago.

Despite the reduced drilling costs, operating costs for generating steam still remains high due to greater heat loss when steam injection is schemed to horizontal well application. Further investigations inquire possibilities to address the solutions to this problem. Chang et al., examined in his simulation study the co-injection with solvent (n-hexane C_6H_{14}) and alternate solvent/steam cycles to reduce total number of cycles. (Chang et al,. 2009).

CSI with Hydraulic Fracturing

The idea of combining cyclic steam stimulation with hydraulic fracturing came out when both steam injection and completion (i.e, sand control completion) techniques generated potential formation damage thus, the permeability near the wellbore creating a choke was lowered that further reduces the oil mobility. Creating fractures allows a more efficient placement of injected steam, heating up larger volume of reservoir and reducing residual oil saturation. This combination is usually considered for low-permeability heavy oil reservoirs like California diatomite (0.1-0.5 md) or Athabasca oil sands (~2.5 d). Several studies reported desirable results (Manrique et al., 1996, and Settari et al., 1981).

Fines and sand production problems are found commonly during cyclic steam injection. The recent study investigated the efficiency of fracturing with viscoelastic surfactant fluid instead of water which worsens the sand and fine production. It was concluded that anionic surfactant fluids minimize gel damage and maintain favourable proppant transportation (Gomez et al., 2012).

Follow Up Methods: Post CSI

CSI is widely used in oil recovery due to its quick response; however, recovery factors are relatively low (10-40% OOIP) compared to other thermal methods such as steam flooding (50-60% OOIP) or in-situ combustion (70-80% OOIP) (Thomas, 2008). This is because the natural energy of the reservoir, as well as oil production, decreases and, when several cycles are reached, oil production tends to decrease even more with decreasing pressure and increasing water production. Consequently, some follow-up processes are used after the implementation of CSI to improve oil recovery, such as CO_2 injection (Luo et al., 2005), steam flooding (Yang, 2007), and air injection as in-situ combustion (Gates et al., 2011, and Hajdo et al., 1985), among others.

One example of CO_2 injection after CSI is in the Lengjiabao heavy oil reservoir, in which CO_2 was injected in extra heavy oil (10,000 -50,000 mPa.s at 50°C) after 3 cycles of CSI with satisfactory results; increasing oil mobility with CO_2 utilization ratio from 3.0 to 6.0 tons oil /tons CO_2 and oil recovery from 10 to 35% (Luo et al., 2005). However, in other wells tested with low permeability, porosity and oil saturation, the injection of CO_2 did not increase oil production.

Another thermal method frequently used as a follow up process for CSI is steam flooding. One of the experiences reported was in the Guantao formation (porosity and permeability relatively high and extra heavy oil with viscosities of 230,000 mPa·s at 50°C) in the Liaohe Oil Field, China, where CSI was applied previously. Steam flooding was adapted by using horizontal wells placed between current vertical CSI wells (Yang, 2007). These vertical wells produced for 3 cycles by CSI and then some of them were switched to steam flood as soon as the horizontal-vertical wells communication was identified. Yang in 2007 reported that the wells have been producing since February 2005 by steam flooding favored by gravity drainage forces. Initially, the predicted oil recovery by CSI was 29% of OOIP, and, with steam flooding follow up after CSS, the forecasted oil recovery was 56% (Yang, 2007).

However, steam flooding is not the right recipe as follow-up after CSI for all types of formations. Every reservoir has its own characteristics such as vertical and horizontal permeabilities, reservoir properties changes caused by CSI, reservoir thickness, and viscosity of the fluids, among others, which have to be evaluated before steam flooding is implemented after CSI (He et al., 1995).

In the Bachaquero-01 reservoir in western Venezuela, CSI has been used since 1965 and currently the production wells have more than 6 cycles. An Extended Cyclic Steam Injection, which is a combination of steam injection and steam flooding, was evaluated numerically. The prediction cases were simulated for 7 cycles of 14 months each and approximately 9 months of steam flooding in different well patters (Chourio et al., 2011). The simulated results showed that there was an additional recovery of 3.7%, reaching the highest recovery in the area of 24.3% of OOIP (Chourio et al., 2011). The pilot test for this project was planned in 2012.

Finally, in-situ combustion performance has also been numerically investigated as a follow up process for CSI (Gates et al., 2011). In Canada, in the Margarite Lake, in wells with a depth of 1476 feet and thickness of 112 feet (Hajdo et al., 1985) and Morgan Field, with wells with a depth of 670 feet and thickness of 30 feet (Marjerrison and Fassihi, 1995), air injection pilots were performed after CSI and the process were proved to be successful (Gates et al., 2011, Hajdo et al., 1985 and Marjerrison and Fassihi, 1995). In addition, CSI was implemented in the Cold Lake oil sands, and the oil recovery was recorded to be 15-20% of the

OOIP (Nzekwu et al., 1990). Consequently, an in-situ combustion process was implemented. The results, presented by Nzekwu et al. showed that the average reservoir temperature and heated zone increased after in-situ combustion which consequently would increase oil recovery. In addition, in the heavy oil reservoir of Midway Field in California, a successful in-situ combustion pilot was conducted in a section subjected to CSI for seven years (Counihan, 1977). The previous CSI cycles helped injectors to prevent burnout, clean the perforations and reduce spontaneous ignition.

Currently, the most used follow up process after CSI is steam flooding. One reason is because it utilizes the installed equipment into the well and on surface which reduces capital cost. However, the most important ground is due to its attribute to sweep the remaining oil to a specific production well. Moreover, CO_2 flooding has been proved to be successful in limited areas and further research must be done to fully develop this technique; likewise, initial investment and CO_2 utilization affects directly capital cost. Finally, air injection has been efficient in some places as well, but it is a process very complicated for simulation and field tested.

Conclusions

- CSI has improved since its discovery in 1959, little number of cycles and low recovery factor have been increased by the use of chemical additives and by better understanding of the geometry and mineralogy of the wells. However, more research needs to be done in understanding relative permeability and wettability changes with temperature at field scale in different formations to increase ultimate oil recovery.
- Cyclic Steam Injection combined with unconventional technologies such as co-injection with chemical additives, horizontal drilling and hydraulic fracturing have been highly successful, improving its conventional recovery factor up to 40%. Recent studies showed that this can be increased even higher.
- Cyclic Steam Injection with horizontal well has had considerable success thanks to reduced directional drilling cost and improved sweep efficiency, although further economic evaluations need to be considered.
- CSI with Hydraulic fracturing has shown good results for low-permeability formation. Further investigation on fracturing fluid needs to be acquired to solve sand productions during the operation.
- In many cases, follow up processes after CSI are convenient solutions to increase reservoir ultimate recovery. However, these processes must be evaluated carefully considering reservoir properties and mineralogy and fluid interaction before fully implemented. In addition, in follow up process selection, economic viability is a major issue, so the increase in oil recovery must be sufficient to cover capital cost and maintain the project profitable during the forecasted time.

Acknowledgment

The authors would like to thank Dr. Berna Hascakir for her guidance and encouragement to write this paper.

References

Adegbesan, K. G. (1992). "Reservoir Simulation Study of a Thermal Horizontal Well Pilot in the Cold Lake Oil Sands." SPE Reservoir Engineering 7(4): 403-406.

Adkins, J. D. (1983). "Field Results of Adding Surfactant to Cyclic Steam Wells." SPE Annual Technical Conference and Exhibition. San Francisco, California, Society of Petroleum Engineers.

Ahmed, Tarek, D., Meehan, and Nathan. (2012). "Advanced Reservoir Management and Engineering (Second Edition)." Pages 541-585.

Ali, Farouq S. M. (1974). "Current Status of Steam Injection as a Heavy Oil Recovery Method." Journal of Canadian Petroleum Technology. Volume 13, Number 1.

Alikhlalov, K. and Dindoruk B. (2011). "Conversion of Cyclic Steam Injection to Continous Steam Injection." SPE Annual Technical Conference and Exhibition. Denver, Colorado, USA, Society of Petroleum Engineers.

Babadagli, T., Er, V., Naderi, K., Burkus, Z., and Ozum, B. (2010). "Use of Biodiesel as an Additive in Thermal Recovery of Heavy Oil and Bitumen." Journal of Canadian Petroleum Technology. Volume 49, Number 11.

Beattie, C.I., Boberg, T.C., and McNab, G.S. (1991). "Reservoir Simulation of Cyclic Steam Stimulation in the Cold Lake Oil Sands." SPE Reservoir Engineering. Volume 6, Number 2.

Blair Jr., C. M., Scribner, R. E., and Stout, C. A. (1982). "Chemical Enhancement of Oil Production by Cyclic Steam Injection." Journal of Petroleum Technology 34 (12): 2757-2762.

Castro, Y. E., Veliz, A. M., Sanchez, D. A., Rodriguez, M. M., Rondon, N. G., Rivero, S., and Cortez, M.L. (2010). "Cyclic Steam Injection with Solvents as Method of Thermal Recovery for Heavy and Extraheavy Oils: Laboratory Tests." Canadian Unconventional Resources and International Petroleum Conference. Calgary, Alberta, Canada, Society of Petroleum Engineers.

Chang, J., Ivory, J., and Rajan, R. S. V. (2009). "Cyclic Steam-Solvent Stimulation Using Horizontal Wells." Canadian International Petroleum Conference. Calgary, Alberta, Petroleum Society of Canada.

Chourio, Geragg; Bracho, Jose and Mohtad, Mehrdad. (2011). "Evaluation and Application of the Extended Cyclic Steam Injection as a New Concept for Bachaquero-01 Reservoir in West Venezuela." SPE 148083-MS.

Cline, V. J. and M. Basham. (2002). "Improving Project Performance in a Heavy Oil Horizontal Well Project in the San Joaquin Valley, California." SPE International Thermal Operations and Heavy Oil Symposium and International Horizontal Well Technology Conference. Calgary, Alberta, Canada.

Counihan, and Thomas M. A. (1977). "Successful In-Situ Combustion Pilot in the Midway-Sunset Field, California." SPE 6525-MS.

Du, J., Brissenden, S.J., McGillivray, P., Bourne, S., Hofstra, P., and Davis, E.J., Roadarmel, W.H., Wolhart, S.L., Marsic, S., Gusek, and R., Wright, C.A. (2005). "Mapping Reservoir Volume Changes During Cyclic Steam Stimulation Using Tiltmeter Based Surface Deformation Measurements." SPE 97848-MS.

Dusseault, M.B. and Rothenburg, L. (2002). "Analysis of Deformation Measurements for Reservoir Management." Oil & Gas Science and Technology – Rev. IFP, Vol. 57. No. 5, pp. 539-554.

Escobar, E., Valko, P., Lee, W. J., and Rodriguez, M.G. (2000). "Optimization Methodology for Cyclic Steam Injection with Horizontal Wells." SPE/CIM International Conference on Horizontal Well Technology. Calgary, Alberta, Canada.

Escrochi, M., Nabipour, M., Ayatollahi, Sh., and Mehranbod, N. (2008). "Wettability Alteration at Elevated Temperatures: The Consequenses of Asphaltene Precipitation." 2008 SPE Internatiomal Symposium and Exibitionon Formation Damage held in Lafayette, Luisiana, USA. SPE 112428.

Gates, Ian D. and Wang, Jacky. (2011). "Evolution of In Situ Oil Sands Recovery Technology in the Field: What Happened and What's New?" SPE 150686-MS.

Gomez, J., Morales, H., Toyo, D., and Bracho, J. (2012). "Fracturing With Viscoelastic Surfactant Fluid in Cyclic Steam Injection Wells - A Synergy for Heavy Oil Recovery." SPE 153536-MS.

Gronseth, J.M. (1989). "Geomechanics Monitoring of Cyclic Steam Stimulation Operations In the Clearwater Formation." International Society for Rock Mechanics IS-1989-166.

Haiyan, H., Shuhong, W., Yitang, Z., Dingmin, W., and Zhong, G. (2005). "State-of-the-Art of Heavy-Oil Development in China and Its Technology Challenges." SPE 10617-MS.

Hajdo, L.E., Hallam, R.J., and Vorndran. (1985). "Hydrogen Generation During In-Situ Combustion." SPE 13661-MS.

He, Z., Zhang, R., Pu, H. Y., and Ren, X. (1995). "The Feasible Conditions Study of Steamflooding for Heavy Oil Reservoirs In China After Cyclic Steam Injection." SPE 30303-MS.

Hongfu, F., Yongjian, L., Liying, S., and Xiaofei, Z. (2002). "The Study on Composition Changes of Heavy oils during Steam Stimulation Processes." ELSEVIER. Fuel 81. p.p 1733-1738 .

Jiang, Q., Thornton, B., Russel-Houston, J., and Spence, S. (2010). "Review of Thermal Recovery Technologies for the Clearwater and Lower Grand Rapids Formations in the Cold Lake Area in Alberta." Journal of Canadian Petroleum Technology. Volume 49, Number 9.

Jones, Jeff and Cawthon, Gary J. (1990). "Sequential Steam: An Engineered Cyclic Steaming Method." Journal of Petroleum Technology. Volume 42, Number 7.

Joshi, S. D. (1991). "Thermal Oil Recovery With Horizontal Wells (includes associated papers 24403 and 24957)." Journal of Petroleum Technology 43(11): 1302-1304.

Khan, Jamaludin and Parag, Dhanpaul. (1992). "Twenty-Five Years of Oil Recovery by Steam Injection." SPE 24198-MS.

Kovscek, A.R., Schembre,, J.M. and Tang, G.-Q. (2008). "Authors' Reply to Discussion of Interrelationship of Temperature and Wettability on the Relative Permeability of Heavy Oil in Diatomaceous Rocks." SPE Reservoir Evaluation & Engineering. Volume 11, Number 3. p.p. 437-438.

Leaute, R. P. and Carey, B. S. (2007). "Liquid Addition to Steam for Enhancing Recovery (LASER) of Bitumen with CSS: Results from the First Pilot Cycle." Journal of Canadian Petroleum Technology. Volume 46, Number 9.

Liguo, Zhong; Shoujun, Zhang; Fei, Wu; Baoshan, Lang; Heng, Liu and Shuai, Gai. (2012). "Improved Heavy-Oil Recovery by Separated-Zones Horizontal-Well Steam Stimulation." Journal of Canadian Petroleum Technology. Volume 51, Number 2.

Luo, R., Cheng, L.-S., and Peng, J.-C. (2005). "Feasibility Study of CO2 Injection for Heavy Oil Reservoir after Cyclic Steam Stimulation: Liaohe oilfield test." SPE 97462-MS.

Manrique, J. F. (1996). "Optimization of Thermal Processes Through Combined Application of Horizontal Wells and Hydraulic Fracturing Technology." International Conference on Horizontal Well Technology. Calgary, Alberta, Canada, Society of Petroleum Engineers, Inc.

Marjerrison, D.M. and Fassihi, M.R. (1995). "Morgan pressure cycling in-situ combustion project: performance and modeling." Geological Society, London, Special Publications. V.84. p. 275-286.

McKay, C., Jones, J., Pomerene, J. (2003). "Successful Horizontal Producers in Midway-Sunset Thermal Operations." SPE Western Regional/AAPG Pacific Section Joint Meeting. Long Beach, California, Society of Petroleum Engineers.

Mendez, Z., Alvarez, J. M., Escobar, E., Colonomos, P., and Campos, P. (1992). "Cyclic Steam Injection With Additives: Laboratory and Field Test Results of Steam/Foam and Steam/Solvent Processes." SPE Annual Technical Conference and Exhibition. Washington, D.C. Society of Petroleum Engineers Inc. SPE 24632-MS

Mendoza, H., Padron, A., and Portillo, F. (1997). "Steam Stimulation In Horizontal Wells Pilot Test In Venezuela." Annual Technical Meeting. Calgary, Alberta, Petroleum Society of Canada.

Miller, Mark A., and Ramey Jr., H.J. (1985). "Effect of Temperature on Oil/Water Relative Permeabilities of Unconsolidated and Consolidated Sands." SPE Journal. Volume 25, Number 6. p.p. 945-953.

Morlot, C. D. and Mamora, D. (2007). "TINBOP Cyclic Steam Injection Enhances Oil Recovery in Mature Steamfloods." Petroleum Society of Canada.

Nzekwu, Ben I., Hallam, Richard J., and Williams, G.J.J. (1990). "Interpretation of Temperature Observations From a Cyclic-Steam/ In-Situ-Combustion Project." SPE Reservoir Engineering. Volume 5, Number 2.

Oil and Gas Journal by Bob Tippee. (2012). "ExxonMobil licenses oil sands steam system." Houston, Feb. 2, 2012. http://www.ogj.com/content/ogj/en/articles/2012/02/exxonmobil-licenses-oil-sands-steam-system.html.

Pahlavan, Hamid and Rafiqul, Islam. (1995). "Laboratory simulation of geochemical changes of heavy crude oils during thermal oil recovery." Journal of Petroleum Science and Engineering. Volume 12, Issue 3, Pages 219–231.

Pollkar, Marcel, Puttagunta, V. R., Decastro, V., Ali, and Farouq S. M.. (1989). "Relative Permeability Curves For Bitumen And Water In Oil Sand Systems." Journal of Canadian Petroleum Technology. Volume 28, Number 1.

Poston, S.W., Ysrael, SHossain, A.K.M.S., Montgomery III, E.F., and Ramey Jr., H.J. (1970). "The Effect of Temperature on Irreducible Water Saturation and Relative Permeability of Unconsolidated Sands." SPE Journal. Volume 10, Number 2. p.p. 171-180.

Prats, Michael. (1978). "A Current Appraisal of Thermal Recovery." Journal of Petroleum Technology. Volume 30, Number 8.

Prats, Michael. (1985). "Thermal Recovery." SPE Monograph Volume 7. Chapter 6. 1985.

Ramey Jr., H. J. A. (1967). "Current Review of Oil Recovery by Steam Injection." SPE 12247.

Ramey Jr., Henry J. (1969). "A Current Look at Thermal Recovery." SPE 2739-MS.

Rao, Dandina N. (1999). "Wettability Effects in Thermal Recovery Operations." SPE Reservoir Eval. & Eng. Vol. 2, No. 5.

Rao, Dandina N., and Karyampudi, R.S. (1999). "Productivity Enhancing Wettability Control Technology for Cicluc Steam Process in the Elk Point Cummings Formation. " Journal of Canadian Petroleum Technology. Special Edition 1999, Volume 38, Number 13.

Reis, J. C. (1990). "Studies of Fractures Induced During Cyclic Steam Injection." SPE California Regional Meeting. Ventura, California, Society of Petroleum Engineers Inc.

Robaina, R. M. and J. L. Ziritt (1988). "Evaluation of a Surfactant: Steam-Soak Pilot Test in the Bolivar Coast, Venezuela." SPE Enhanced Oil Recovery Symposium. Tulsa, Oklahoma, 1988.

Schembre, J.M., Tang, G.-Q., and Kovscek, A.R. (2006). "Interrelationship of Temperature and Wettability on the Relative Permeability of Heavy Oil in Diatomaceous Rocks (includes associated discussion and reply)." SPE Reservoir Evaluation & Engineering. Volume 9, Number 3. p.p. 239-250.

Scott, J. D., S. Proskin, A., and Adhikary, D. P. (1994). "Volume And Permeability Changes Associated With Steam Stimulation In an Oil Sands Reservoir." Journal of Canadian Petroleum Technology. Volume 33, Number 7.

Settari, A. and J. M. Raisbeck. (1981). "Analysis and Numerical Modeling of Hydraulic Fracturing During Cyclic Steam Stimulation in Oil Sands." Journal of Petroleum Technology 33 (11): 2201-2212.

Shu, W. R. and K. J. Hartman. (1988). "Effect of Solvent on Steam Recovery of Heavy Oil." SPE Reservoir Engineering 3(2): 457-465.

Speight, J. G. (2007). "The Chemistry and Technology of Petroleum." CRC Press/Taylor & Francis. 4th Edition, Volume 114, Chapter 6.

Srivastava, P. and Castro, L. U. (2011). "Successful Field Application of Surfactant Additives to Enhance Thermal Recovery of Heavy Oil." SPE Middle East Oil and Gas Show and Conference. Manama, Bahrain, Society of Petroleum Engineers.

Taraskin, Evgeniy; Ursegov, Stanislav; Pechor, N., Muliak, Vladimir; Chertenkov, Mikhail, and Alabushin, Andrey. (2012). "Thirty Years of Experience in the Application of Thermal Methods of Heavy Oil Recovery in the Permian-Carboniferous Reservoir of the Usinsk Field." SPE 160759-MS.

Thomas, S. (2008). "Enhanced Oil Recovery – An Overview." Oil & Gas Science and Technology – Rev. IFP, Vol. 63. No. 1, pp. 9-19.

Trebolle, R. L., Chalot, J. P., and Colmenares, R. (1993). "The Orinoco Heavy-Oil Belt Pilot Projects and Development Strategy." SPE International Thermal Operations Symposium. Bakersfield, California, Society of Petroleum Engineers, Inc.

Valera, Cesar A., Escobar, Manuel A., and Iturbe, Yrene J. (1999). "Use of Surfactants in Cyclic Steam Injection in Bachaquero-01 Reservoir." SPE 54020-MS.

Walters, D.A., Settari, A., and Kry, P.R. (2000). "Poroelastic Effects of Cyclic Steam Stimulation in the Cold Lake Reservoir." SPE 62590-MS.

Walters, D.A., Settari, A., and Kry, P.R. (2002). "Coupled Geomechanical and Reservoir Modeling Investigating Poroelastic Effects of Cyclic Steam Stimulation in the Cold Lake Reservoir." SPE Reservoir Evaluation & Engineering. Volume 5, Number 6.

Wong, R. C. K. and Li, Y. (2001). "A Deformation-Dependent Model for Permeability Changes in Oil Sand due to Shear Dilation." Journal of Canadian Petroleum Technology. Volume 40, Number 8.

www.netl.doe.gov. *"FIG. 1* CYCLIC STEAM INJECTION PROCESS." United States Department of Energy, Washington D.C.

Xia, T. X., Greaves, M. (2006). "In Situ Upgrading of Athabasca Tar Sand Bitumen Using THAI." Chemical Engineering Research and Design, Volume 84, Issue 9, September 2006, page 856-864

Yale, David P., Mayer, Todd, and Wang, Jianlin. (2010). "Geomechanics of Oil Sands under Injection." American Rock Mechanics Association 10-257.

Yang, L. (2007). "Field Test of SAGD as Follow-Up Process to CSS in Liaohe Oil Field of China." Journal of Canadian Petroleum Technology. Volume 46, Number 4.

Yongtao, Sun, Lichang, Zhao, Liguo, Zhong, Di, and Yu, Lin. (2011). "Enhance Offshore Heavy Oil Recovery by Cyclic Steam-Gas-Chemical Co-stimulation." SPE 149831-MS.

Yuan, Yanguang, Xu, Bin, and Yang, Baohong. (2011). "Geomechanics for the Thermal Stimulation of Heavy Oil Reservoirs-Canadian Experience." SPE 150293-MS.

Zhang, X., Zhang, Y., Yue, Q., Gao, Y., and Shen, D. (2009). "Conformance Control of CSS and Steam Drive Process with a Carbamide Surfactant." Journal of Canadian Petroleum Technology. Volume 48, Number 9.

Johannes Alvarez is a PhD student at Texas A&M University in Petroleum Engineering. He holds a B.Sc. degree from Universidad Simon Bolivar, Venezuela, and a M.Sc. degree from Stanford University, USA, both in Chemical Engineering. His research interests include fracture fluid performance with surfactant additives in oil shale, enhance oil recovery in shale formations, surface chemistry, and X-Ray tomography methods. Previously, he worked for 11 years in Petroleos de Venezuela S.A. (PDVSA) as Process and Infrastructure Engineer, Production Engineering Superintendent, Production Engineering District Manager and lately as Planning Division Manager. Mr. Alvarez is a member of the Society of Petroleum Engineers.

Sungyun Han, Goyang Gyeonggi, Republic of Korea, is a MSc student in Petroleum Engineering at Texas A&M University, College Station, Texas. He is currently researching on in-situ combustion process. His research interests include seismic interpretation and numerical modeling of thermal enhanced oil recovery. He received a B.Sc. degree of Petroleum Engineering from Texas A&M University, College Station, Texas, in 2012. He has worked as a teaching assistant in Department of Petroleum Engineering, instructing laboratory assignments of numerical methods used in oil and gas industry. He is also a research assistant in Ramey's Thermal Laboratory where he is conducting thermal EOR, In-situ combustion, experiments. Mr. Han is a member of the Society of Petroleum Engineers.

Quantification of Rock Porosity Changes before and after Freezing

Jun He[1], Peng Pei[2], Kegang Ling[3], Zhengwen Zeng[4], and Hong Liu[5]

[1,2,4,5] Geology and Geological Engineering Department, University of North Dakota
Grand Forks, ND, USA, 58202

[3]Petroleum Engineering Department, University of North Dakota
Grand Forks, ND, USA, 58202

[1]jun.he@my.und.edu; [2]peng.pei@engr.und.edu; [3]kegang.ling @engr.und.edu; [4]zane.zeng @engr.und.edu; [5]hong.liu @engr.und.edu

Abstract

Petroleum exploration and production from shale formations have gained great momentum throughout the world in the last decade. Producing hydrocarbons from shale is challenging because of the low porosity and permeability thus requiring fracturing completion, whose successes rely on the knowledge of rock properties and in-situ stress. It is imperative to investigate and understand the rock geomechanics in the shale formations. To the best of our knowledge, the freezing method is the most successful approach to prepare the shale core sample for lab test. Unfortunately, the preparation of shale core plugs includes the procedure of freezing that alters the rock properties. This paper quantifies the difference in rock porosity before and after the freezing based on data from numerous rock experiments. Porosities of different rocks had been measured before the rock samples were put into the freezer for freezing. After the rock porosities have been measured, the core samples were stored in the freezer. Then the porosities of core samples after freezing were measured. With above experiments, a porosity database was built and a non-linear regression method was used to derive correlations to quantify the changes in the porosity due to freezing. Our correlations is applicable for geoscientists and engineers to adjust the shale property to the values before freezing. With the correct porosity, more accurate original oil in place can be estimated and more reliable permeability from porosity-permeability correlation can be calculated. Eventually, the estimated ultimate recovery can be evaluated confidently. Results of this study can also be applied to other areas such as underground storage of liquid natural gas (LNG), underground energy storages, etc.

Keywords

Rock Porosity; Freezing of Rock; Rock Porosity Change

Introduction

After more than one hundred years of development and production, conventional oil and gas reserves are depleting significantly on a worldwide basis. In order to meet the increasing demand of hydrocarbon energy, it is essential to develop unconventional resources. Shale oil and gas becomes crucial supplements to the conventional hydrocarbon reservoirs. Petroleum exploration and production from shale formations have gained great momentum throughout the world in the last decade. Producing hydrocarbons from shale is challenging because of the low porosity and permeability thus requiring fracturing completion, whose successes rely on the knowledge of rock properties and in-situ stress. It is imperative to investigate and understand the rock geomechanics in the shale formations. Although numerous investigations have been conducted to better understand rock properties of shale and the fluids properties and flow behavior in shale under reservoir condition, the progresses in rock and fluid characterizations and fluid-rock interaction description are impeded by the availability of experimental data on shale sample. Our literature review indicates that numbers of core analysis on shale are limited due to the difficulty in preparing shale plug from drilling cores. The brittle nature of shale makes the successful rate of preparing plug from drilling core lower. Usually, the successful rate ranges from 0 to 10%. Another element that contributes to the rare experimental data of shale is the low porosity and extremely low permeability feature of shale. Conventional methods to analyze core porosity and permeability do not work or cannot be afforded due to expensive cost and time consuming when they are applied to analyze shale. To overcome the sampling difficulty, the freezing sample method is used in preparing the plug for core analysis. It is undoubted that the freezing will alter the rock texture and

structure thus the rock properties such as porosity and permeability, but to the best of our knowledge, it is the most successful approach to prepare the shale core sample for lab tests. Therefore, to obtain original rock properties, it is imperative to quantify the difference before and after the freezing. In this study, the way the porosity changes during freezing process has been investigated.

The effect of temperature on elastic properties of porous materials has been investigated by researchers of different fields, including petroleum engineering, civil engineering, and chemical engineering. For the purposes of this study, we reviewed the studies that focused on the porosity change as a function of temperature. These researches can be classified into two main categories according to temperature below and above ice melting point (or water freezing point). The first category targeted temperature higher than ice melting point (or water freezing point); while the other investigated temperature is lower than ice melting point under which the expansion of ice becomes the main cause that alters the rock properties. Followings list some important researches identified as milestones that advance the understanding of effect of temperature on rock properties.

First Category: Temperature Higher than Ice Melting Point

Somerton et al. (1965) studied the thermal effect on sandstone in the range of 400 to 800°C, whose works showed that large changes in physical properties occur as a result of heating and subsequent cooling to room temperature. They believed that the alteration of rock properties is caused by a number of reactions occurring during heating, which include the differential thermal expansion of the quartz grains, the dissociation of dolomite at higher temperatures, and the "firing" of clays at lower temperatures. Sanyal et al. (1974) investigated the effect of temperature on petrophysical properties of reservoir rocks. From their literature review, there was no definite result known about the effect of temperature on porosity. The bulk volume increases slightly (<1%) with temperature increase up to 200°C. However, a cubic pore model was analyzed to simulate the change in pore structure due to thermal expansion of mineral grains and cement. The expansion of the grain spheres and the quartz cement due to temperature increase was calculated using the thermal expansion coefficients of quartz. Different degrees of cementation were considered in the model. Changes of pore radius at different temperature levels were obtained by subtracting new cement thickness from new grain radius. Vodak et al. (2004) studied the effect of temperature on strength-porosity relationship for concrete material at various temperatures ranging from 25 to 280°C. Their study depicted that the increment of porosity as a result of microcracking is mainly due to thermal incompatibility of hardened cement paste and aggregate during heating. Tian et al. (2004) obtained similar results in their experimental studies on sandstone, claystone, clayey sandstone, and sandy claystone where specimens were heated up to 1000°C. It was observed that cracks were generated on the rock samples, especially claystone, due to the difference in thermal expansion properties of different minerals in the rock. Yao et al. (2012) and Hu et al. (2012) presented further investigations on the microcracking mechanism during the procedure of heating rock and coal samples. In general, at the initial heating stage, the rise of temperature leads to the expansion of rock matrix, but the temperature is not high enough to generate microcracks. Therefore, at the initial heating stage, the porosity would slightly drop, or keep constant because of expansion of matrix and the inelastic property preventing restoration of deformation when specimens are cooled to ambient temperature. As the temperature continuously increases, the induced thermal stress reaches and exceeds the strength of matrix, thus leading to the generation of microcracks and increase of porosity. Therefore, a "threshold temperature" exists, where the sudden jump of porosity is observed, as the thermal stress becomes higher than the matrix strength and creates cracks in rocks. Yuan et al. (2012) conducted experimental study and simulated the effect of temperature on the voids in cement under high pressure and temperature conditions.

Second Category: Temperature Lower than Ice Melting Point

Other studies have paid attention to the effect of freezing on rock properties. Hundere (1984) investigated the changes of unconsolidated core properties after freezing. Kindt (1985) studied the effect of freezing on permeability of unconsolidated sandstone through experimental measurement. Torsaeter and Beldring (1987) analyzed the effect of freezing on the permeabilities of unconsolidated to slightly consolidated rocks and core plugs. Increment

in porosity, which ranges from 0.7% to 9.6%, was observed in their experimental data. Neaupane et al. (1999) presented a coupled thermo-hydro-mechanical model to simulate the freezing and thawing process. Their study focused on the effect of phase change of pore water on the deformation of material. No discussion of the change of porosity by freezing is available in the paper. Coussy (2005) studied the poromechanics of freezing materials with the focus on the liquid saturation degree as a function of temperature, and ice-dependent poroelastic properties.

From the descriptions above, most of the previous researches focused on the high temperature effect, or the effect of phase change of the pore water on the matrix structure in freezing process. The induced thermal stress due to freezing may result in fractures. It is expected that a "threshold temperature" exists during freezing, where sudden change of porosity due to fracturing would be observed. Some of aforementioned researches compared the rock or specimen porosity before and after freezing, and the porosity change with the variation of temperature. Unfortunately, it is unfeasible to measure shale porosity before freezing due to its brittle nature. To drill plug from shale core successfully, the core needs to be frozen. Therefore quantification of porosity change resulting from freezing is highly desirable for the sake of obtaining original shale porosity. In this study, the difference has been quantified in rock porosity before and after the freezing based on experimental data from numerous rock specimens. To do so, porosities of the samples were measured before they were frozen. Then samples were stored in freezer and frozen at temperatures of -13.8 and -85°C for more than one week. After that they were taken out of freezer and allowed to return to temperature of 20°C. Their porosities were measured again once temperature reached equilibrium.

Equipment, Measurement Principle, and Procedure

Equipment

Gas compression method is used to measure the porosities of specimens in this work. Fig. 1 shows the setup to measure rock porosity. The system consists of gas source, three pressure gauges, and two chambers. The core is put in Chamber 2.

Measurement Principle

The measurement principle is based on real gas law. Followings are the derivation of governing equation to measure the core porosity.

Firstly, the sum of the volume of Chamber 1 and pipeline volume between Gas Inlet Valve and Gas Outlet Valve is denoted as Volume 1, V_1.

$$V_1 = V_{\text{chamber 1}} + V_{\text{pipeline between Gas Inlet Valve and Gas Inlet Valve}} \quad (1)$$

Similarly, the sum of the volume of Chamber 2 (without core) and pipeline volume between Gas Outlet Valve and Gas Vent Valve is denoted as Volume 2, V_2.

$$V_2 = V_{\text{chamber 2}} + V_{\text{pipeline between Gas Outlet Valve and Gas Vent Valve}} \quad (2)$$

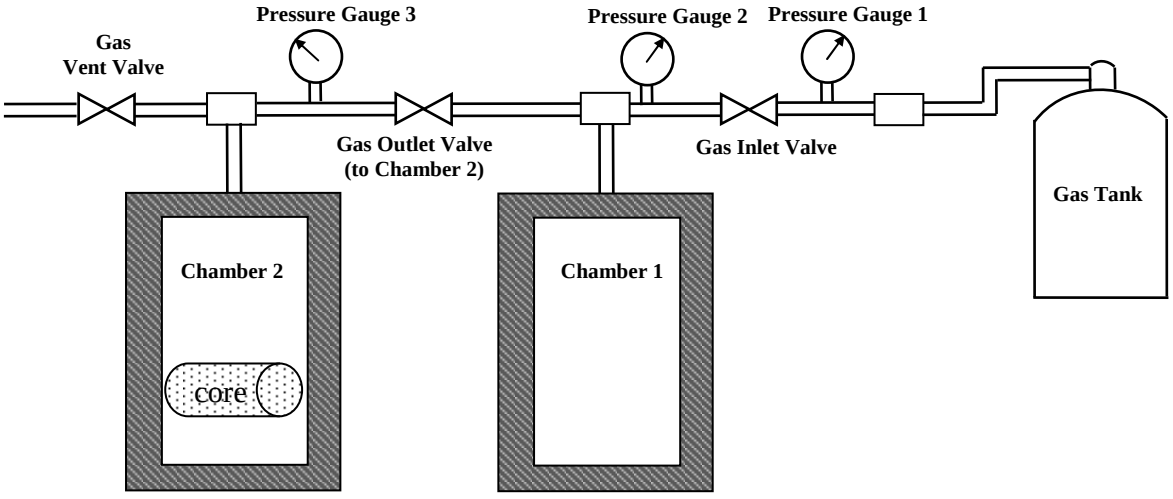

FIG. 1 SCHEMATIC OF FACILITY TO MEASURE ROCK POROSITY

The bulk volume of core is denoted as $V_{bulk,,\,core}$ which is calculated by

$$V_{bulk,core} = \frac{\pi}{4} D_{core}^2 h_{\text{core}} \tag{3}$$

Initially, the pressure in Chamber 1 is p_1 and pressure in Chamber 2 is p_2, where $p_1 > p_2$. Then Gas Outlet Valve is open to allow gas flow from Chamber 1 to Chamber 2 and reach equilibrium. The equilibrium pressure, p_3, is recorded. According to real gas law we have

$$p_1 V_1 = z_1 n_1 R T_1 \tag{4}$$

$$p_2 \left[V_2 - V_{bulk,core} \left(1-\phi\right) \right] = z_2 n_2 R T_2 \tag{5}$$

$$p_3 \left\{ \left[V_2 - V_{bulk,core} \left(1-\phi\right) \right] + V_1 \right\} = z_3 \left(n_1 + n_2\right) R T_3 \tag{6}$$

The temperature is kept constant and pressure is changed in a narrow range. Therefore we have

$$z_1 \cong z_2 \cong z_3 \tag{7}$$

Equations (4), (5), and (6) can be simplified into

$$p_1 V_1 = z_1 n_1 R T_1 \tag{8}$$

$$p_2 \left[V_2 - V_{bulk,core} \left(1-\phi\right) \right] = z_1 n_2 R T_1 \tag{9}$$

$$p_3 \left\{ \left[V_2 - V_{bulk,core} \left(1-\phi\right) \right] + V_1 \right\} = z_1 \left(n_1 + n_2\right) R T_1 \tag{10}$$

Summing Equations (8) and (9) we obtain

$$p_2 \left[V_2 - V_{bulk,core} \left(1-\phi\right) \right] + p_1 V_1 = z_1 \left(n_1 + n_2\right) R T_1 \tag{11}$$

Comparing the right-hand-sides of Equations (10) and (11) we have

$$\begin{aligned} & p_2 \left[V_2 - V_{bulk,core} \left(1-\phi\right) \right] + p_1 V_1 \\ & = p_3 \left\{ \left[V_2 - V_{bulk,core} \left(1-\phi\right) \right] + V_1 \right\} \end{aligned} \tag{12}$$

Rearranging Equation (12) yields

$$\phi = 1 - \frac{V_2}{V_{bulk,core}} + \frac{\left(p_1 - p_3\right) V_1}{\left(p_3 - p_2\right) V_{bulk,core}} \tag{13}$$

Equation (13) is the governing equation to measurement rock porosity. Three pressures are recorded in the measurement. Volume 1, V_1, and Volume 2, V_2 can be determined using standard volume samples made of stainless steel (zero porosity). The approach is also based on real gas law. The bulk volume of core can be readily calculated from core diameter and height.

Measurement Procedure

The measurement of porosity of a specimen includes following steps:

1) Put the core into Chamber 2, close Gas Vent Valve, and open Gas Inlet Valve and Gas Outlet Valve to allow gas from gas tank fill Chambers 1 and 2 until pressure reaches 100 psig
2) Open Gas Vent Valve and allow gas from gas tank purge Chambers 1 and 2, keeping 10 to 20 minutes until the purity of gas in Chambers 1 and 2 is high enough.
3) Close Gas Vent Valve, Gas Inlet Valve, and Gas Outlet Valve, record the pressure of Chamber 2, p_2.
4) Keep Gas Vent Valve and Gas Outlet Valve close, Open Gas Inlet Valve and allow gas from gas tank fill Chamber 1 until its pressure reaches target pressure, close Gas Inlet Valve and record the pressure of Chamber 1, p_1.
5) Open Gas Outlet Valve to allow gas flow from Chamber 1 to Chamber 2 (because $p_1 > p_2$), wait until pressure reaches equilibrium, or pressure at Pressure Gauge 3 equates pressure at Pressure Gauge 2, record equilibrium pressure, p_3.
6) Now the porosity measurement of specimen has been completed. Porosity can be calculated by Equation (13).

Two series of different size specimens were used in this work, the first of which has a dimension of 1-in. diameter by 2-in. length, and another has a dimension of 2-in. in diameter by 4-in. in length. The porosities of rock before and after freezing were measured. The procedure of our experiment is:

1) Measure the porosity of rock at temperature of 20 ^{o}C before frozen.
2) Put the specimen into freezer and freeze it at temperature of -13.8^{o}C for one week, then take it out of freezer and allow specimen temperature return to 20^{o}C. Then measure specimen porosity again.
3) Put the specimen into another freezer and freeze it at temperature of -85^{o}C for one week, then take it out of freezer and allow specimen temperature return to 20^{o}C. Then measure specimen porosity

one more time.

Upon finishing the procedure we obtain three porosities for each specimen: one before freezing, one after freezing at -13.8°C, and one after freezing at -85 °C.

Experimental Results Analysis and Development of Correlations

To demonstrate the change of porosity by freezing distinctly, the relative porosity change is calculated using porosity of rocks at 20°C as the base. Table 1 shows the experiment results.

Based on the test data, three kinds of porosity change by freezing can be identified as shown in Fig. 2, and correspond to different types of rocks. For the first type (a), whose lithology is shaly sandstone, the porosity increases as the rock has been frozen, and reaches maximum at temperature barely lower than zero. After that, local maximum, porosity declines as temperature is reduced further. For the second type (b), whose lithology is clean sandstone, the trend is similar to first type but with smaller change. The porosity change by freezing is very small until temperature reaches the "threshold temperature", beyond that point the porosity begins to increases quickly. The third type (c), whose lithology is sandstone with high calcium carbonate concentration, follows the same trends as first and second types. A local maximum porosity is seen at temperature barely lower than zero, but the change of porosity lies between first and second types. A "threshold temperature" also can be found as the temperature decreases continuously. When the temperature is lower than the "threshold temperature", the porosity increases again.

Three equations corresponding to three rock types are listed below:

a:

$$y = -2.6\times10^{-6}\ x^3 - 4.0\times10^{-4}\ x^2 - 1.13\times10^{-2}\ x + 0.48 \quad (14)$$

b:

$$y = -3.6\times10^{-7}\ x^3 - 2.2\times10^{-5}\ x^2 + 7.6\times10^{-5}\ x + 0.01 \quad (15)$$

c:

$$y = -2.9\times10^{-6}\ x^3 - 2.0\times10^{-4}\ x^2 + 3.4\times10^{-3}\ x + 0.049 \quad (16)$$

where x is temperature and y is the relative porosity change.

Discussions

Porosity change is the combined effects of expansion of the water inside the core due to phase change and the contractions of the matrix of the core and ice. When the core is stored in freezer at temperature lower than freezing point, the freezing causes the water inside the core to expand due to the fact that ice occupies a larger volume than liquid water. The relative volume change is

$$\frac{\Delta V_{\text{expansion}}}{V_{water}} = \frac{V_{ice} - V_{water}}{V_{water}} = 8.7\% \quad (17)$$

The expansion volume due to water phase change is

$$\Delta V_{\text{expansion}} = 0.087 V_{water} = 0.087\phi S_w V_{bulk,core} \quad (18)$$

During the freezing both ice and rock matrix contract. The volume change due to the contraction can be estimated using the thermal expansion coefficient. The contraction volumes of ice and rock matrix are calculated by

$$\begin{aligned}\Delta V_{\text{contraction,ice}} &= V_{\text{ice}}\left(T_{\text{freezing point}} - T_{\text{freezer}}\right)\alpha_{\text{ice}} \\ &= 1.087\phi S_w V_{bulk,core}\left(T_{\text{freezing point}} - T_{\text{freezer}}\right)\alpha_{\text{ice}}\end{aligned} \quad (19)$$

and

$$\begin{aligned}\Delta V_{\text{contraction,matrix}} &= \sum_i^n V_{i,\text{mineral}}\left(T_{\text{freezing point}} - T_{\text{freezer}}\right)\alpha_{i,\text{mineral}} \\ &= V_{bulk,core}\left(1-\phi\right)\sum_i^n f_{i,\text{mineral}}\left(T_{\text{freezing point}} - T_{\text{freezer}}\right)\alpha_{i,\text{mineral}}\end{aligned} \quad (20)$$

respectively.

where

$$\alpha_{\text{ice}} = 50\times10^{-6}\ 1/^{\circ}\text{C}$$

and the coefficients of thermal expansion of different minerals are listed in Table 2.

Combining Equations (18), (19), and (20) we have the total volume change, which is

$$\begin{aligned}\Delta V_{total} &= \Delta V_{\text{contraction,ice}} + \Delta V_{\text{contraction,matrix}} - \Delta V_{\text{expansion}} \\ &= V_{bulk,core}\begin{bmatrix} 1.087\phi S_w\left(T_{\text{freezing point}} - T_{\text{freezer}}\right)\alpha_{\text{ice}} \\ +\left(1-\phi\right)\sum_i^n f_{i,\text{mineral}}\left(T_{\text{freezing point}} - T_{\text{freezer}}\right)\alpha_{i,\text{mineral}} \\ -0.087\phi S_w \end{bmatrix}\end{aligned} \quad (21)$$

TABLE 1 SPECIMEN DATA AND CHANGE OF POROSITY CAUSED BY FREEZING

Samples	Diameter	Length	Porosity Φ(%)			(Φ-Φ20)/Φ20		
	mm	mm	20 °C	-13.8 °C	-85 °C	20 °C	-13.8 °C	-85 °C
1	23.54	42.25	12.512	19.197	14.127	0.000	0.534	0.129
2	24.3	51.55	10.969	14.472	14.579	0.000	0.319	0.329
3	24.65	28.44	16.624	21.496	18.006	0.000	0.293	0.083
4	24.69	49.98	11.296	13.764	12.620	0.000	0.218	0.117
5	24.25	52.58	12.755	14.770	13.886	0.000	0.158	0.089
6	24.38	52.69	13.504	14.968	14.168	0.000	0.108	0.049
7	24.67	55.25	16.481	17.941	18.068	0.000	0.089	0.096
8	24.69	52.6	13.501	14.694	14.470	0.000	0.088	0.072
9	24.95	51.05	18.478	20.029	18.870	0.000	0.084	0.021
10	24.73	51.56	18.807	20.302	19.698	0.000	0.079	0.047
11	24.82	51.55	15.057	15.976	15.531	0.000	0.061	0.031
12	38.44	76.15	13.999	14.759	14.574	0.000	0.054	0.041
13	24.65	58.38	17.068	17.952	17.770	0.000	0.052	0.041
14	38.08	74.33	12.958	13.583	13.784	0.000	0.048	0.064
15	38.43	76	13.382	14.006	13.832	0.000	0.047	0.034
16	38.43	76.26	14.868	15.534	15.574	0.000	0.045	0.047
17	24.45	53.91	22.483	23.485	23.491	0.000	0.045	0.045
18	38.48	76.18	12.114	12.652	12.090	0.000	0.044	-0.002
19	38.42	76.25	13.699	14.209	14.493	0.000	0.037	0.058
20	38.25	75.21	13.212	13.646	13.804	0.000	0.033	0.045
21	38.47	74.14	13.728	14.125	13.931	0.000	0.029	0.015
22	24.76	46.6	12.995	13.364	14.038	0.000	0.028	0.080
23	38.38	75.77	13.778	14.138	13.951	0.000	0.026	0.013
24	25	51.95	15.194	15.569	16.415	0.000	0.025	0.080
25	38.42	76.26	13.802	14.134	14.209	0.000	0.024	0.029
26	24.63	50.37	22.060	22.566	24.060	0.000	0.023	0.091
27	24.81	49.62	15.094	15.311	15.583	0.000	0.014	0.032
28	38.44	76.05	14.238	14.350	14.268	0.000	0.008	0.002
29	24.3	52.37	12.875	12.953	15.676	0.000	0.006	0.218
30	24.27	52.95	17.583	17.684	18.736	0.000	0.006	0.066
31	50.12	102.78	14.963	15.028	14.905	0.000	0.004	-0.004
32	38.47	76.14	12.412	12.426	12.603	0.000	0.001	0.015
33	50.27	105.05	15.611	15.591	15.491	0.000	-0.001	-0.008
34	38.3	75.81	13.334	13.279	13.177	0.000	-0.004	-0.012
35	38.2	76.15	13.547	13.453	13.512	0.000	-0.007	-0.003
36	50.16	102.78	15.057	14.910	14.936	0.000	-0.010	-0.008
37	25.68	50.31	21.884	21.660	22.118	0.000	-0.010	0.011
38	50.24	103.43	15.681	15.510	15.562	0.000	-0.011	-0.008
39	38.46	76.03	14.976	14.803	14.600	0.000	-0.012	-0.025
40	38.35	76.25	14.156	13.959	14.192	0.000	-0.014	0.003
41	38.46	78.17	16.881	16.635	16.845	0.000	-0.015	-0.002
42	24.78	50.78	16.586	16.338	16.901	0.000	-0.015	0.019
43	24.47	48.81	11.164	10.917	15.535	0.000	-0.022	0.392
44	24.84	48.97	15.599	15.234	15.533	0.000	-0.023	-0.004
45	38.45	76.15	14.352	13.970	13.954	0.000	-0.027	-0.028
46	24.5	52.55	15.155	14.658	15.408	0.000	-0.033	0.017
47	24.08	51.48	15.224	14.713	15.698	0.000	-0.034	0.031
48	24.17	50.09	9.821	9.386	13.411	0.000	-0.044	0.366
49	24.74	51.49	16.681	15.858	17.042	0.000	-0.049	0.022
50	24.58	51.65	13.062	12.199	15.665	0.000	-0.066	0.199
51	24.83	51.85	16.718	15.605	16.960	0.000	-0.067	0.014
52	24.8	50.45	15.283	14.235	17.547	0.000	-0.069	0.148
53	24.65	52.67	12.503	11.583	15.378	0.000	-0.074	0.230
54	24.17	50.45	11.694	10.684	13.892	0.000	-0.086	0.188
55	24.4	52.27	11.843	10.799	13.288	0.000	-0.088	0.122
56	24.25	52.56	13.886	12.305	16.040	0.000	-0.114	0.155

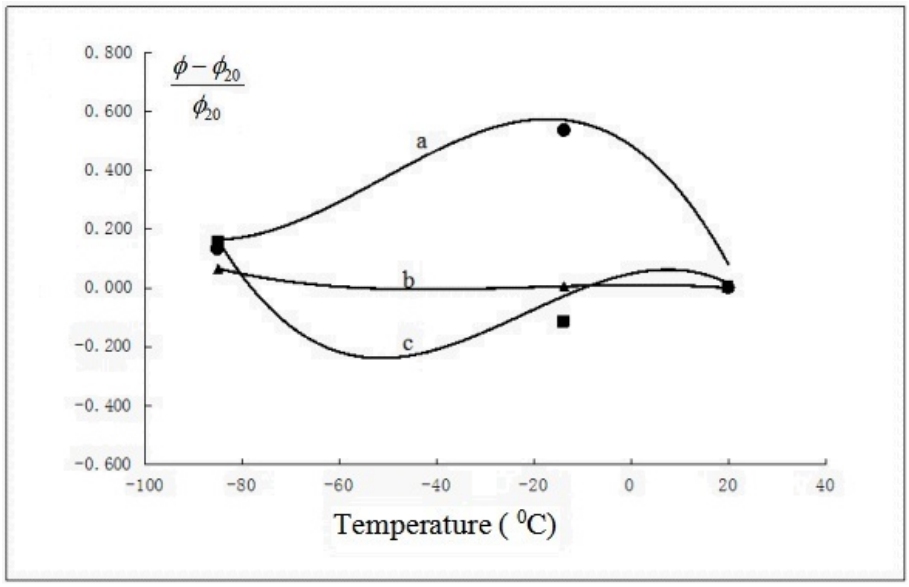

FIG. 2 REGRESSION ANALYSIS OF CHANGE OF POROSITY CAUSED BY FREEZING

TABLE 2 THERMAL EXPANSION COEFFICIENTS OF COMMON MINERALS IN ROCK

Mineral	Thermal Expansion Coefficient	Reference
Quartz	0.77~1.4×10^{-6} 1/^{o}C	http://www.engineeringtoolbox.com/linear-expansion-coefficients-d_95.html
Alkali Feldspar	14~17×10^{-6} 1/^{o}C	Hovis, G., et al., 2008, A simple predictive model for the thermal expansion of AlSi$_3$ feldspars.
Plagioclase Feldspar	10~17×10^{-6} 1/^{o}C	Tribaudino, M., et al., 2010, Thermal expansion of plagioclase feldspars:
Calcium Carbonate	6~9×10^{-6} 1/^{o}C	http://www.supercivilcd.com/THERMAL.htm
Calcium Carbonate	8×10^{-6} 1/^{o}C	http://www.engineeringtoolbox.com/linear-expansion-coefficients-d_95.html

Therefore, the relative volume change is

$$\frac{\Delta V_{total}}{V_{bulk,core}} = \begin{bmatrix} 1.087\phi S_w \left(T_{\text{freezing point}} - T_{\text{freezer}}\right)\alpha_{\text{ice}} + \\ (1-\phi)\sum_i^n f_{i,\text{mineral}} \left(T_{\text{freezing point}} - T_{\text{freezer}}\right)\alpha_{i,\text{mineral}} \\ -0.087\phi S_w \end{bmatrix} \tag{22}$$

Equation (22) gives the incremental porosity at freezer temperature. So the rock porosity at freezer temperature is

$$\phi_{freezer\ temperature} = \phi + \begin{bmatrix} 1.087\phi S_w \left(T_{\text{freezing point}} - T_{\text{freezer}}\right)\alpha_{\text{ice}} \\ +(1-\phi)\sum_i^n f_{i,\text{mineral}} \left(T_{\text{freezing point}} - T_{\text{freezer}}\right)\alpha_{i,\text{mineral}} \\ -0.087\phi S_w \end{bmatrix} \tag{23}$$

If the induced stress is less than the adhesive strength of rock and the rock is elastic, the rock should restore to its original condition when the temperature is restored to original temperature. Unfortunately, no rock is completely elastic. Therefore, rock cannot restore to its original condition exactly even the rock is not damaged by the induced stress. The residual porosity difference as a result of freezing-unfreezing cycle depends on the water and the percentage of inelastic component in rock.

If the induced stress is higher than the adhesive strength of rock, rock porosity after freezing-unfreezing cycle will be larger than the original porosity because the microcracks and plastic component in the rock prevent the rock from restoring to original condition when temperature return to original value. To evaluate the occurring of microcrack, it is necessary to introduce the definition of volumetric strain, which is defined as the ratio of the change in volume of the body to its original volume (Jaeger, et al., 2007).

$$\varepsilon_{\text{V}} = \frac{\Delta V}{V_{\text{original}}} \tag{24}$$

Recalling that the volumetric strain is the sum of the three principal normal strains, we have

$$\varepsilon_V = \varepsilon_1 + \varepsilon_2 + \varepsilon_3 \quad (25)$$

The relationships between the three principal normal stresses and strains give us

$$\sigma_1 = \lambda\varepsilon_V + 2G\varepsilon_1 \quad (26)$$

$$\sigma_2 = \lambda\varepsilon_V + 2G\varepsilon_2 \quad (27)$$

$$\sigma_3 = \lambda\varepsilon_V + 2G\varepsilon_3 \quad (28)$$

Summing up the three principal stresses gives

$$3\tau_m = \sigma_1 + \sigma_2 + \sigma_3 = (3\lambda + 2G)\varepsilon_V \quad (29)$$

The mean stress is related to the volumetric strain through

$$\tau_m = \left(\lambda + \frac{2}{3}G\right)\varepsilon_V = \left(\lambda + \frac{2}{3}G\right)\begin{bmatrix} 1.087\phi S_w\left(T_{\text{freezing point}} - T_{\text{freezer}}\right)\alpha_{\text{ice}} + \\ (1-\phi)\sum_i^n f_{i,\text{mineral}}\left(T_{\text{freezing point}} - T_{\text{freezer}}\right)\alpha_{i,\text{mineral}} \\ -0.087\phi S_w \end{bmatrix} \quad (30)$$

where

$$\lambda = \frac{2Gv}{1-2v} \quad (31)$$

If the mean stress calculated from Equation (30) is higher than adhesive strength of rock, micorcrack will be created and increase in porosity will be expected.

Analysis of experimental data indicates that there is a "threshold temperature" for rock. When the rock is frozen at temperature high than "threshold temperature" and restored to original temperature, porosity decreases. Otherwise, porosity increases. At temperature between freezing point and "threshold temperature", the expansion resulting from phase change from water to ice dominates over the contractions of rock matrix and ice. The expanded volume is larger than the contracted volume. The deformation occurring at this temperature range is partially inelastic and the rock cannot restore to original condition even temperature is restored to original temperature. It should be noted that the induced stress is below the adhesive strengths between cements and grains or the strength of matrix under this temperature range. At temperature lower than the "threshold temperature", the contractions of ice and rock matrix dominates over the expansion due to the water phase change. The induced thermal stress resulting from strain caused by contraction reaches and exceeds the adhesive strengths between cements and grains or the strength of matrix, thus leading to the creation of microcracks. These microcracks are the main reason for the increment of porosity. Under such condition, the expanded volume is smaller than the contracted volume. The deformation is damaging and irreversible, and again the rock cannot restore to its original condition after temperature is restored to original temperature. Obviously, the "threshold temperature" is a function of rock type, rock structure, texture, mineral composition, rock strength, water saturation, mineral hydration, and porosity. To calculate an accurate porosity change, it is necessary to know the volumetric fraction of minerals in rock, as well as the coefficient of thermal expansion of each mineral.

Conclusions

Following conclusions can be drawn upon finishing this study:

There is a "threshold temperature" for every specific rock. If the rock is frozen at temperature high than "threshold temperature", porosity will decrease. Otherwise, porosity will increase.

The "threshold temperature" is a function of rock type, rock structure, texture, mineral composition, rock strength, water saturation, mineral hydration, and porosity.

At temperature between freezing point and "threshold temperature", the expansion resulting from water phase change to ice dominates over the contraction of rock matrix. The expanded volume is larger than the contracted volume. The deformation occurring at this temperature range is partially inelastic and the rock cannot restore to original condition completely even temperature is restored to original value.

At temperature lower than the "threshold temperature", the contractions of ice and rock matrix dominates over the expansion due to the water phase change. The stress resulting from strain caused by contraction exceeds the adhesive strengths between cements and grains, thus leading to the creation of microcracks which are the main reason of the increase in porosity. Under such condition, the expanded volume is smaller than the contracted volume. The deformation is damaging and irreversible, and again the rock cannot restore to original condition after temperature is returned to original value.

Three empirical correlations related to three rock types

have been developed to estimate the porosity change before and after freezing.

ACKNOWLEDGMENT

The authors are grateful to Petroleum Engineering Department in University of North Dakota. This research is supported in part by the U.S. Department of Energy (DOE) under award number DE-FC26-08NT0005643 and North Dakota EPSCoR Program under award number EPS-0814442, as well as Wilson M. Laird Core and Sample Library and North Dakota Geological Survey for providing core samples for this study.

NOMENCLATURE

D_{core} = core diameter

$f_{i,mineral}$ = volumetric fraction of mineral *i* in total matrix

G = shear modulus

h_{core} = length of core

n_1 = gas moles in Chamber 1

n_2 = gas moles in Chamber 2

p_1 = pressure at Chamber 1

p_2 = pressure at Chamber 2

p_3 = pressure at Chambers 1 and 2 after pressure reaches equilibrium

R = universal gas constant

S_w = water saturation

T_1 = temperature at Chamber 1

T_2 = temperature at Chamber 2

T_3 = temperature at Chambers 1 and 2 after pressure reaches equilibrium

$T_{freezer}$ = freezer temperature

$T_{freezing\ point}$ = water freezing temperature

V_1 = volume of chamber 1 + pipeline volume between Gas Inlet Valve and Gas Outlet Valve

V_2 = volume of chamber 2 (without core) + pipeline volume between Gas Outlet Valve and Gas Vent Valve

$V_{chamber\ 1}$ = volume of chamber 1

$V_{chamber\ 2}$ = volume of chamber 2 (without core)

$V_{bulk,\ core}$ = bulk volume of core

V_{ice} = ice volume

$V_{original}$ = original volume

$V_{pipeline\ volume\ between\ Gas\ Inlet\ Valve\ and\ Gas\ Outlet\ Valve}$ = pipeline volume between Gas Inlet Valve and Gas Outlet Valve

$V_{pipeline\ volume\ between\ Gas\ Outlet\ Valve\ and\ Gas\ Vent\ Valve}$ = pipeline volume between Gas Outlet Valve and Gas Vent Valve

V_{water} = water volume

v = Poisson's ratio

z_1 = gas z-factor at Chamber 1

z_2 = gas z-factor at Chamber 2

z_3 = gas z-factor at Chambers 1 and 2 after pressure reaches equilibrium

ΔV = volume change

$\Delta V_{expansion}$ = expansion volume due to water phase change

$\Delta V_{contraction,ice}$ = ice contraction volume

$\Delta V_{contraction,\ matrix}$ = matrix contraction volume

$\Delta V_{i,,mineral}$ = mineral i contraction volume

ΔV_{total} = total volume change

α_{ice} = coefficient of thermal expansion of ice

$\alpha_{i,mineral}$ = coefficient of thermal expansion of mineral *i*

ϕ = porosity, or original porosity

$\phi_{freezer\ temperature}$ = porosity at freezer temperature

$\phi_{original}$ = original porosity

ε_1 = first principal normal strain

ε_2 = second principal normal strain

ε_3 = third principal normal strain

ε_V = volumetric strain

σ_1 = first principal normal stress

σ_2 = second principal normal stress

σ_3 = third principal normal stress

τ_m = mean stress

REFERENCES

Coussy, O. 2005. Poromechanics of freezing materials. *Journal of the Mechanics and Physics of Solids* 53: 1689-1718.

Hu, X., Liang, W., and Hou, S., et al. 2012. Experimental study of effect of temperature and stress on

permeability characteristics of raw coal and shaped coal. *Chinese Journal of Rock Mechanics and Engineering*, 31 (6): 1222-1229.

Hundere, I. 1984. The Effect of Freezing on Unconsolidated Core Material from Troll Field. Internal paper, Saga Petroleum A/S, Oslo, 1984.

Jaeger, J. Cook, N. G., and Zimmerman, R. 2007. *Fundamentals of Rock Mechanics*, 4th edition, Malden, MA: Blackwell Pub., 2007.

Kindt, R.K. 1985. The Effect of Freezing on Permeability of Unconsolidated Sandstones – An Experimental Investigation. *Norwegian Institute of Technology, Trondheim, Norway, 1985.*

Neaupane, K., Yamabe, T. and Yoshinaka, R. 1999. Simulation of a fully coupled thermo-hydro-mechanical system in freezing and thawing rock. *International Journal of Rock Mechanics and Mining Sciences*, 36: 563-580.

Sanyal, S., Marsden, S. and Ramey, H., 1974. Effect of temperature on petrophysical properties of reservoir rocks. Paper SPE 4898 presented at the SPE California Regional Meeting, San Francisco, California, 4-5 April.

Somerton, W.H., Mehta, M.M. and Dean, G.W. 1965. Thermal Alteration of Sandstones. *Journal of Petroleum Technology*, May 1965: 589-593.

Tian, H., Kempka, T. and Schluter, R., et al. 2009. Influence of high temperature on rock mass surrounding *in situ* coal conversion sites. Proceedings of the 10th International Symposium on Environmental Geotechnology and Sustainable Development, Bochum, Germany, 7-11 September.

Torsaeter, O. and Beldering, B. 1987. The effect of freezing of slightly consolidated cores. *SPE Formation Evaluation*, 2 (3): 357-360. Paper SPE 14300-PA.

Vodak, F., Trtik, K. and Kapickova, O., et al. 2004. The effect of temperature on strength – porosity relationship for concrete. *Construction and Building Materials*, 18: 529-534.

Yao, T., Li, J. and Huang, Y. 2012. Effects of temperature and stress on porosity and permeability reservoir. *Journal of Shenzhen University Science and Engineering*, 29 (2):154-158.

Yuan, Z., Schubert, J., Teodoriu, C., and Gardoni, P. 2012. HPHT Gas Well Cementing Complications and its Effect on Casing Collapse Resistance. Paper SPE153986 presented at the SPE Oil and Gas India Conference and Exhibition, 28-30 March 2012, Mumbai, India.

Jun He is a graduate student at the University of North Dakota. His research interests are in the area of reserve evaluation and reservoir characterization. He holds a BS degree from Southwest Petroleum University in geology and an MS degree from China University of Petroleum in petroleum engineering.

Peng Pei is a research engineer at the Institute of Energy Studies, University of North Dakota. He holds a Ph.D. in Geological Engineering from University of North Dakota, and an M.S Mechanical Engineering from University of North Dakota. He also has a B.S. in Mechanical Engineering from North China Electrical Power University. His research area focuses on energy-related rock mechanics.

Kegang Ling is an assistant professor in Petroleum Engineering at University of North Dakota. His research interests are in the area of production optimization. He holds a BS degree from the China University of Petroleum in geology, an MS degree from University of Louisiana at Lafayette, and a PhD degree from Texas A&M University, both in petroleum engineering.

Zhengwen Zeng is an associate professor in Geological Engineering at University of North Dakota. His research interests are in the area of geomechanics. He holds a BS and MS degree in Engineering Geology from Southwest Jiaotong University, China, and a PhD degree in Petroleum & Geological Engineering from University of Oklahoma.

Hong Liu is a lab technician in Geological Engineering at University of North Dakota. She holds a BS degree in Mechanical Engineering from Southwest Jiaotong University, China and an MS degree in Science of Business from New Mexico Institute of Mining and Technology.

Processing and Interpretation of Permanent Downhole Monitoring Data

Fei Wang*[1], Xiaogang Li[2]

*[1]Institute of Petroleum Engineering, China University of Petroleum, Beijing, 102249, China

[2]Sinopec International Petroleum Exploration and Production Corporation, Beijing, 100029, China

*[1]wangfei@cup.edu.cn

Abstract

In recent years, permanent down-hole gauge (PDG) has been widely installed in oilfields around the world to monitor the reservoir and well conditions in real time. Continuous monitoring of pressure enables engineers to observe ongoing changes in the well and makes operating adjustments accordingly to enhance oil and gas recovery. Transient pressure monitored by PDG are characterized with long term and high volume data which are inherently noisy, full of variable-rate superposition and multi-well interference effects. These effects make the monitoring pressure trends decline or rise and then obscure or distort the traditional flow behavior, which makes the following analysis difficult. This paper has presented a systematic methodology that tackled the issues related to the permanent down-hole monitoring data, utilizing both the wavelet transform and multi-well deconvolution techniques. With this developed method, the outlier information in PDG data can be extracted. The variable-rate superposition and inter-well interference effects can be removed at the same time. Moreover, hundreds of pressure events i.e. bulidups and drawdowns can be detected and reconstructed to reflect reservoir properties and connectivity across the reservoir. The whole workflow for processing and interpretation of permanent down-hole monitoring data is proposed in this paper. Field case study is performed to demonstrate these procedures. The study results prove that the developed method works well in processing and interpretation of long-term permanent down-hole monitoring data.

Keywords

Permanent Down-Hole Gauge; Reservoir Monitoring; Wavelet Transform; Deconvolution Transform; Data Processing

Introduction

Permanent down-hole gauges (PDG) are metering devices installed down-hole to monitor the well and reservoir conditions in real time. Technology has evolved over more than 40 years since the first installation (Chorneyko, D.M., et al., 2006). Installation of these gauges has been an increasingly common industry practice worldwide because of the improved reliability and the value of information that the gauges provide. PDG components include gauges, housing, cable, connections, and acquisition systems, as shown in Fig.1. Permanent monitoring systems measure and record well performance and reservoir behavior from sensors which are placed downhole during the completion. These measurements give engineers information essential to dynamically manage hydrocarbon assets, allowing them to optimize production techniques, diagnose problems, refine field development and adjust reservoir models. Sensors are placed downhole with the completion string close to the heart of the reservoir. Modern communications provide direct access to sensor measurements from anywhere in the world. Reservoir and well behaviors may now be monitored easily in real time, 24 hours a day, day after day, throughout the lifetime of the reservoir. Engineers can catch performance daily, examine responses to changes in production or secondary recovery processes and also have a record of events to help diagnose problems and monitors in a power plant's control room (Athichanagorn, Suwat, et al, 1999; Frota, H.M. and Destro, W., 2006) .

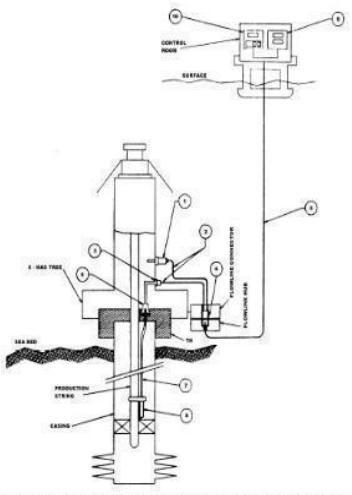

FIG.1 PERMANENT DOWNHOLE GAUGE

Data from permanent down-hole gauges can be examined and collected almost as soon as they are acquired at the down-hole of the well. A wide range of

application of permanent downhole gauge data has been reported in the oil and gas industry (Ouyang, L.B. and Kikani, J., 2002; McCracken, M. and Chorneyko, D., 2006; Tibold, M.P., et al., 2000; Queipo, N.V., et al., 2002; Gringarten, A.C., et al., 2003). These applications include: reduction on ambiguity and uncertainties in the interpretation; detection of the changes in reservoir properties; monitoring of skin, permeability, pressure drawdown over time; monitoring of hydraulic fracturing operations; pump inlet and outlet pressures for pumping wells; evaluation on the performance of well completion, simulation or workover; identification of reservoir connectivity; evaluation on operational efficiency; reduction on the flowback time of new wells; and assistance in reservoir simulation and history matching.

In practice, there are issues associated with the data that these gauges collect. Large amounts of data are gathered continuously at intervals down to one second over several years, as shown in Fig.2. This data contains more information about the reservoir parameters changing during short and long time intervals than data from traditional pressure transient tests which last for relatively small durations. In this situation, more information will be hidden in this long-term PDG pressure record than just a collection of drawdowns and buildups, which makes the interpretation of PDG data a new challenge.

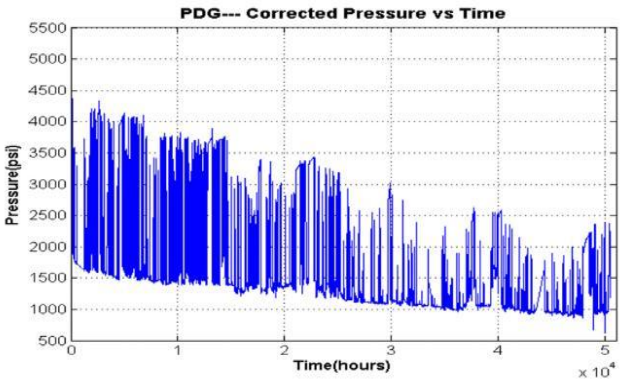

FIG. 2 PERMANENT DOWNHOLE GAUGE DATA

Besides the characteristic of long term and large volume, there are several issues related to this kind of PDG pressure data, such as the data are inherently noisy because they are obtained under uncontrolled conditions. Moreover, it involves two key effects in the transient pressure data from permanent down-hole gauges, namely, multi-rate superposition and multi-well interference effects. Multi-well interference effect, a very common in PDG pressure data in oilfield practice (Britt, L.K., et al., 1991; Erwin, M.D., et al., 2002), makes the measured pressure trends decline or rise and then obscures or distorts the traditional flow behavior, which makes the following analysis difficult, i.e. the construction of the incorrect semi-log straight line or the incorrect radial flow regime on a pressure derivative log-log plot.

These issues have motivated several studies in data processing, noise reduction and new interpretation methodologies for the permanent down-hole gauge data. Xiaogang Li(2009) proposed a wavelet based data processing and interpretation procedure. Fei Wang (2010) presented a deconvolution based method for multi-rate superposition and well interference extraction. In this paper, the above two methodologies are organized and integrated into a newly released procedure for processing and interpretation of PDG data. This procedure was presented as a multiple-step methodology that tackled the different issues related to the data acquired from permanent down-hole gauges.

Workflow for Processing and Interpretation of PDG Data

The newly released workflow for permanent down-hole gauge data includes four procedures, shown in Fig.3. In collecting data, the focus is tried on the dynamic data, especially PDG pressure and production data. Then the PDG data was processed and analyzed in three different ways: wavelet-based welltesting, deconvolution-based welltesting and numerical welltesting. Finally, all the results were integrated by means of future history match. The target is to apply PDG data to improve the reservoir model.

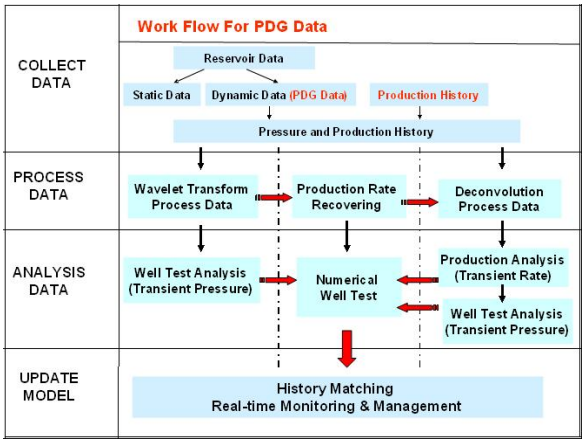

FIG. 3 WORKFLOW FOR PROCESSING AND INTERPRETATION OF PDG DATA

The workflow follows two ways and reaches the same goal. One way, shown on left side of the picture, uses

the wavelet-based welltest to analyse the data in order to get the changed parameter of reservoir property. The main drawback of this way is to handle the noise and huge amounts of data before the welltest analysis is implemented. The wavelet transform proved to be an effective approach to solve this problem just concentrates on each flow regime of the reservoir behaviour.

The other way, shown on right side of the picture, uses the whole test sequence in the welltest analysis by deconvolution processing. This approach gives much higher estimates on the test area without any flow regime or reservoir geometry limitations. Multi-rate superposition and well interference problems in PDG data can be solved in this procedure.

The result of the analytical well test gives the range which is the first guess of the reservoir parameters. Then the near well model is validated by numerical well testing. This part model is integrated with the whole reservoir model to achieve the true reservoir model. This workflow includes two main techniques i.e wavelet-based data processing and deconvolution-based data processing. The detailed methodologies are presented as follows.

PDG Data Processing Technique

The data processing technique involves two approaches i.e. wavelet and deconvolution, which prepare the PDG data for the following well test analysis. The procedure will first divide the whole PDG data into separated buildup (BU) and drawdown (DD). The wavelet transform is applied to identify the event of outlier, BU and DD in the high frequency signal. Then the separated BU and DD sequence without outlier will be deconvolved to achieve multi-rate normalization and interference extraction. The final step is to compress and smooth data in order to get the trend of derivative in the log-log plot. The data is compressed according to the variety of signal. More data points will be kept when the signal changed significantly. And the sample interval is allocated according to the log scale. The compressed signal is still noised in the log-log plot. So, further smooth data is necessary to clean derivative. Lowess and loess method will be used to smooth these data. During this processing procedure, the different issues related to the PDG data can be tackled.

Theory Background of Wavelet Transform

A wavelet, a wave-like oscillation with an amplitude that starts at zero, and increases, and then decreases back to zero, can typically be visualized as a "brief oscillation" like one might see recorded by a seismograph or heart monitor. In mathematics, a wavelet series is a representation of a square-integrable function by a certain orthonormal series generated by a wavelet.

The integral wavelet transform is the integral transform defined as

$$[W_\psi f](a,b) = \frac{1}{\sqrt{|a|}} \int_{-\infty}^{\infty} \overline{\psi(\frac{x-b}{a})} f(x)dx \quad (1)$$

The wavelet coefficients c_{jk} are then given by

$$c_{jk} = [W_\psi f](2^{-j}, k2^{-j}) \quad (2)$$

Here, a = 2 − j is called the binary dilation or dyadic dilation, and b = k2 − j is the binary or dyadic position.

The continuous wavelet transform (CWT) is defined as the sum over all time of the signal multiplied by scaled, shifted versions of the wavelet function ψ:

$$C(scale, position) = \int_{-\infty}^{\infty} f(t)\Psi(scale, position, t)dt \quad (3)$$

The results of the CWT are many wavelet coefficients C, which are a function of scale and position. Scaling a wavelet simply means stretching (or compressing) wavelet, shown in Fig.4.

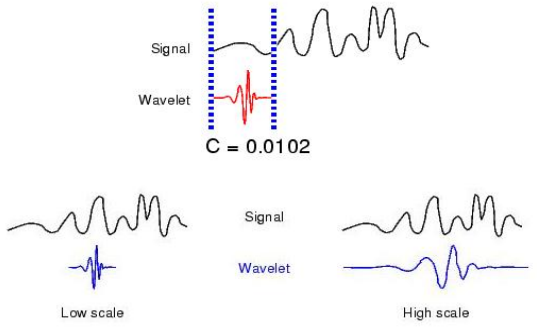

FIG. 4 DIAGRAM OF CONTINUOUS WAVELET TRANSFORM

The first discrete wavelet transform(DWT) was invented by the Hungarian mathematician Alfréd Haar. For an input represented by a list of 2n numbers, the Haar wavelet transform may be considered to simply pair up input values, storing the difference and passing the sum. This process is repeated recursively, pairing up the sums to provide the next scale: finally resulting in 2n − 1 differences and one final sum.

The Haar wavelet's mother wavelet function ψ(t) can be described as

$$\psi(t)=\begin{cases}1 & 0\le t<1/2,\\ -1 & 1/2\le t<1,\\ 0 & otherwise.\end{cases} \quad (4)$$

Its scaling function $\phi(t)$ can be described as

$$\phi(t)=\begin{cases}1 & 0\le t<1,\\ 0 & otherwise\,.\end{cases} \quad (5)$$

Mathematically, the wavelet can be used to extract information from many different kinds of data, because it will resonate if the unknown signal contains information of similar frequency.

Wavelet-based PDG data Processing

Wavelet-based processing approach allows the use of long time intervals where more precise low-frequency information is desirable, and shorter regions where high-frequency information is desirable. While an advantage of using haar wavelets is for the analysis of signals with sudden transitions, just like the PDG data with outliers.

The outlier which is isolated and lies away from the rest of the PDG data can cause discontinuities in the data stream creating two consecutive singularities. For example, an outlier that lies above the trend of the data departs from the data trend, creating the first singularity. The second singularity is a result of a sudden decrease from the outlier back to the trend of the signal. This characteristic can be exploited using a singularity detection frame with wavelets. When an outlier exist, the detail signal will first change sharply in one direction, either increasing or decreasing, and then change again in the opposite direction. Therefore, the singularities created by the outliers can be detected by screening for two large magnitudes of the detail signal with opposite signs. In order to determine the outliers, a threshold is set up for the magnitude of the detail signal.

Generally, a complete record of times at which the well flow rate change is not available. Fortunately, the times at which the flow rates change can be determined by identification of sudden changes in pressure data. These changes can be viewed as singularities in the data. Therefore, the wavelet modulus maximal, which indicates the neighborhoods of singularities, can be used to determine the times at which flow rate changes, then the BU can be separated from the DD.

The procedure of wavelet method to process and analyze PDG data has shown in Fig.5. First, the data evaluation will be applied to know the distribution of data point. Second, detection of algorithm will release the separated BU and DD without outlier. Third, individual BU and DD are compressed and denoised in order to get the high quality signal in log-log plot. At last, the signal is plotted in the log-log plot for analysis.

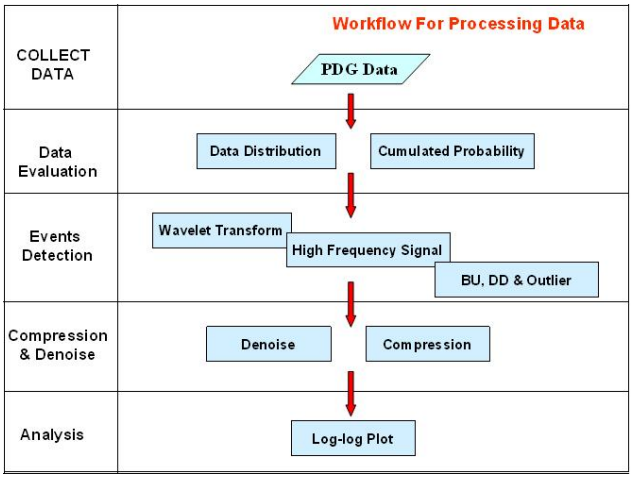

FIG.5 WAVELET-BASED PDG DATA PROCESSING

The procedure to detect event is as follows:

- Calculation on the data distribution of detail signal can help to get the first guess for threshold in identifying the event.
- This threshold is used to get all high frequency signals which include DD, BU and outlier.
- Classify these data into different group. If the group size is small, this may be the outlier. And these data values of original signal are required to check.
- if the group size is big (more than 1min), this can be considered as the begin of BU or DD. Then the original data in the both side of group need to be checked as well. This can identify the BU and DD.
- Then if the group is the beginning of BU, then check the distribution of the following data of group to identify the shut-in-BU or rate-drop-BU.

Theoretical Background of Deconvolution Transform

Hypothesis: $h(t)$ is a linear response of a system, the output is $y(t)$ and input is $x(t)$.

So $y(t)$ can be written as a convolution integral as follows:

$$y(t) = \int_{-\infty}^{\infty} h(t-\tau)x(\tau)d\tau \tag{6}$$

With given output $y(t)$ and input $x(t)$ to recover the system response $h(t)$ is so-called Deconvolution. Once the convolution integral (Eq.6) is applied to single-well problem, it turns to be Duhamel principle:

$$\Delta p(t) = p_i - p_{wf}(t) = \int_0^t q(\tau)\frac{dp_u(t-\tau)}{dt}d\tau \tag{7}$$

Where, $q(t)$ and $p_{wf}(t)$ are the measured flow rate and bottom-hole pressure. p_i is the initial pressure and p_u is the unit-rate pressure response, referred to as the impulse response of the reservoir system.

It is assumed that there are n active wells in a reservoir and these wells are in good connectivity with each other. When using $x = 1,2,\ldots, n$ to denote each of these wells, the total bottom-hole pressure drop of well x can be expressed as follows:

$$p_x(t) = p_i - \int_0^t q_x(t-\tau)\frac{dp_{uxx}(\tau)}{dt}d\tau - \sum_{y=1}^{n}\int_0^t q_y(t-\tau)\frac{dp_{uxy}(\tau)}{dt}d\tau$$
$$(x \in n, y \in n, x \neq y) \tag{8}$$

It means that the down-hole pressure drop measured in one well benefits from not only its self-production but also the production of other active wells in the same reservoir. And the relationship follows superposition principle.

In the multi-well convolution function above, p_{uxx} represents the pressure response at the down-hole of well x due to the production itself, while p_{uxy} represents the interference response, namely the pressure response at the down-hole of well x due to the unit-rate production of well y. Multi-well deconvolution is to extract the self and interference information from the total dataset.

Deconvolution-based PDG data processing

Deconvolution-based processing approach can convert a series of transient pressure, due to variable or step rate history into an equivalent unit-pressure transient rate. The interference information can be extracted as well from the total pressure response data. Namely, multi-well deconvolution removes the effects of well rate variation and of the interferences from other wells operating in the reservoir and reconstructs the characteristic pressure transient response to unit-rate production of each active well in the reservoir. These deconvolved responses to unit-rate production reflect reservoir properties and connectivity across the reservoir. Recovery of this information early in the life of the field through integrated analysis of dynamic pressure data provides an opportunity to adjust and optimize reservoir development plans.

The procedure of multi-well decovolution method to process and analyze PDG data has been shown in Fig.6.

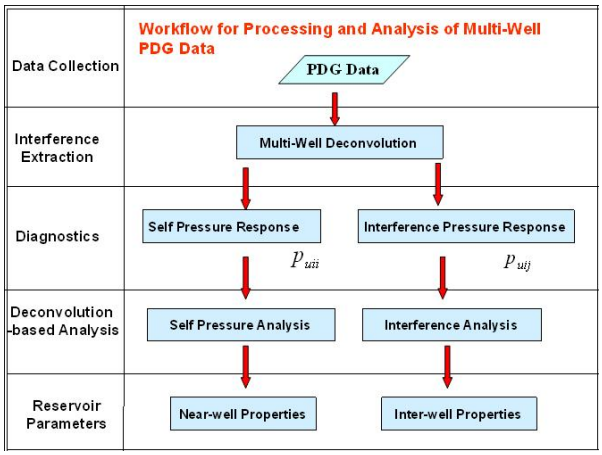

FIG. 6 DECONVOLUTION-BASED PDG DATA PROCESSING

Firstly, the multi-well deconvolution transform algorithm has been employed to extract the well interference from the total pressure response and get the decomposed well self pressure response p_{uii} and the well interference response p_{uij}. Finally deconvolution-based self pressure analysis could be used to obtain near-well properties and interference analysis of the extracted p_{uij} could be carried out to reveal inter-well properties.

Field Example

The purpose of this simple example is to illustrate the procedures of the wavelet and deconvolution approaches. Fig.7(a) displays the history of permanent down-hole gauge test in North sea field. The dataset of this example is one month data which is about 30,000 data points.

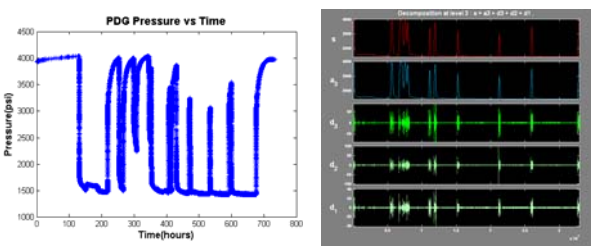

(a) (b)

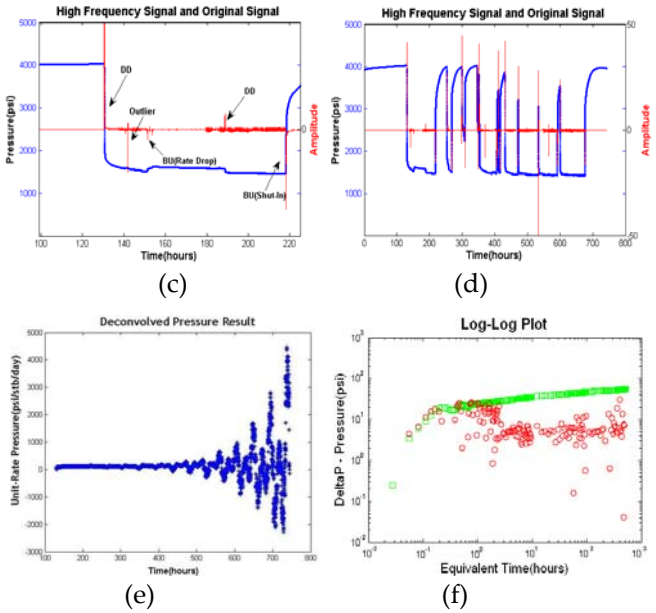

FIG.7 PROCESSING AND INTERPRETATION OF PDG DATA

As stated above, wavelet transform can decompose the original signal into different level wavelet signal in different frequency. In Fig.7(b) , the red curve is the original signal. The haar wavelet, used to decompose the original into four level signals (d1, d2, d3 and a3), is found to be available to identify the event in PDG data because the signal is step change during the event happens. d1, d2, and d3 are all high frequency signal, while the a3 is low frequency signal. The three detail signal (d1, d2 and d3) reflect the high frequency part of signal. However, here we just use the highest frequency detail signal to detect event because the high frequency gives high resolutions. As shown in Fig.7(c), the blue line is the original pressure data and the red line is the highest frequency signal of original signal. Any events can cause a sharp change in the high frequency. The value of these events in the high frequency is more than zero. And this can be used to distinguish the different type events.

Fig.7(c) shows some events which can be identified based on high frequency signal with our algorithm. The principle is that the value of high frequency is positive when DD happens and the values are negative when BU happens. And both will happen when the outlier is met. But this rule is just suitable for ideal case or low frequency recorded data. However, for this case study, the algorithm need consider more condition to distinguish these 33 events i.e. all the BUs and DDs caused by the rate change, shown in Fig.7(d).

Then multi-well deconvolution algorithm is implemented on the pressure BUs and DDs without outlier. The interference pressure response is extracted and the self pressure response is obtained simultaneously, shown in Fig.7(e). Fig.7(f) shows the deconvolved self pressure and its derivative on log-log plot. Three flow regimes are clearly identified by the derivative curve. Thereafter, traditional pressure transient analysis can be used to calculate the reservoir parameters.

Conclusions

This paper systematically introduces permanent down-hole gauge system and data. The characteristic of PDG data is long-term and large-volume, inherently noisy, full of multi-rate superposition and multi-well interference effects.

For this reason, the paper presents a systematic methodology for processing permanent down-hole gauge data, utilizing both the wavelet transform and multi-well deconvolution techniques. Wavelet transform extracts the outlier information from the PDG data, detects the pressure events and separates the BUs from the DDs. Recovery of this information early in the processing procedure is necessary and significant for the post-process results.

Multi-well deconvolution removes the effects of well rate variation and interferences from other wells operating in the reservoir and reconstructs the characteristic pressure transient response to unit-rate production of each active well in the reservoir. Deconvolved responses reflect reservoir properties and connectivity across the reservoir. Recovery of this information through integrated analysis of dynamic pressure data provides an opportunity to get more well and reservoir information.

Field example shows the power of our algorithms to process long term PDG data with the integrated methodology presented in this paper. The whole workflow provides the industry engineers a framework for reservoir monitoring and testing through permanent down-hole gauges.

Acknowledgment

The author would like to thank Science Foundation of China University of Petroleum, Beijing (No.YJRC-2011-02) for the financial support during this research.

References

Athinichanagorn, Suwat: "Development of an interpretation methodology for long-term data from permanent

downhole gauges", PhD thesis, Standford University, Department of Petroleum Engineering, 1999.

Britt, L.K., Jones, J.R., Pardinl, R.E., and Plum, G.L., "Reservoir Description by Interference Testing of the Clayton Field,"SPE 19846, 1991.

D.M. Chorneyko:" Real-Time Reservoir Surveillance Utilizing Permanent Downhole Pressures- An Operator's Experience," paper SPE 103213 presented at the 2006 SPE Annual Technical Conference and Exhibition, 24-27. September, San Antonio, Texas, USA.

Erwin,M.D.,Sander, L.Allen.s., Redman , R.Scott.," Multiwell Interference Test in the Colville River Field, Alaska", SPE 77453, 2002.

Fei Wang: "Processing and Analysis of Transient Pressure from Permanent Down-hole Gauges", PhD thesis, Heriot-Watt University, Insititute of Petroleum Engineering, 2010.

Gringarten, A.C., Schroeter, Thomas von, Rolfsvaag, T., and Bruner, J.,"Use of Downhole Permanent Pressure Gauge Data to Diagnose Production Problems in a North Sea Horizontal Well", SPE 84470, 2003.

H. M. Frota and W. Destro: "Reliability Evolution of Permanent Downhole Gauges for Campos Basin Subsea Wells: A 10-Year Case Study," paper SPE102700 presented at the 2006 SPE Annual Technical Conference and Exhibition, 24-27 September, San Antonio, Texas, USA.

M. McCracken and D. Chorneyko: "Rate Allocation Using Permanent Downhole Pressures,"paper SPE 103222 presented at the 2006 SPE Annual Technical Conference and Exhibition, 24-27 September, San Antonio, Texas, USA.

Ouyang, Liang-Biao., and Kikani, J., "Improving Permanent Downhole Gauge (PDG) Data Processing via Wavelet Analysis", SPE 78290, 2002.

Queipo, N.V., Verde, A., Goicochea, J., Romero, D., Zambrano, A., and Bracho, A.,"Applications of Permanent Downhole Pressure, Temperature, and Flow Rate Measurements for Reservoir Description and Production Optimization: a Taxonomy, Processes, and Benefits", SPE 77897, 2002.

Tibold, M.P., Simonian, S., Chawla, M., Akbar, M.,"Well Testing with a Permanent Monitoring System", paper SPE 63079 presented at the 2000 SPE Annual Technical Conference and Exhibition, 1-4 October, Dallas, Texas, USA.

Xiaogang Li: "Processing Transient Pressure from Permanent Down-hole Gauges", PhD thesis, Heriot-Watt University, Insititute of Petroleum Engineering, 2009. Conference and Exhibition, 1-4 October, Dallas, Texas, USA.

Xiaogang Li: "Processing Transient Pressure from Permanent Down-hole Gauges", PhD thesis, Heriot-Watt University, Insititute of Petroleum Engineering, 2009.